MNRAS **471,** 3529–3546 (2017)
Advance Access publication 2017 July 6
doi:10.1093/mnras/stx1697

The planetary nebula IC 4776 and its post-common-envelope binary central star

Paulina Sowicka,[1★] David Jones,[2,3] Romano L. M. Corradi,[2,4] Roger Wesson,[5] Jorge García-Rojas,[2,3] Miguel Santander-García,[6] Henri M. J. Boffin[7] and Pablo Rodríguez-Gil[2,3]

[1]*Nicolaus Copernicus Astronomical Center, Bartycka 18, PL-00-716 Warsaw, Poland*
[2]*Instituto de Astrofísica de Canarias, E-38205 La Laguna, Tenerife, Spain*
[3]*Departamento de Astrofísica, Universidad de La Laguna, E-38206 La Laguna, Tenerife, Spain*
[4]*GRANTECAN, Cuesta de San José s/n, E-38712 Breña Baja, La Palma, Spain*
[5]*Department of Physics and Astronomy, University College London, Gower Street, London WC1E 6BT, UK*
[6]*Observatorio Astronómico Nacional (OAN-IGN), C/Alfonso XII, 3, E-28014 Madrid, Spain*
[7]*European Southern Observatory, Karl Schwarzschild Strasse 2, D-85748 Garching, Germany*

Accepted 2017 June 29. Received 2017 June 26; in original form 2017 May 31

ABSTRACT

We present a detailed analysis of IC 4776, a planetary nebula displaying a morphology believed to be typical of central star binarity. The nebula is shown to comprise a compact hourglass-shaped central region and a pair of precessing jet-like structures. Time-resolved spectroscopy of its central star reveals a periodic radial velocity variability consistent with a binary system. Whilst the data are insufficient to accurately determine the parameters of the binary, the most likely solutions indicate that the secondary is probably a low-mass main-sequence star. An empirical analysis of the chemical abundances in IC 4776 indicates that the common-envelope phase may have cut short the asymptotic giant branch evolution of the progenitor. Abundances calculated from recombination lines are found to be discrepant by a factor of approximately 2 relative to those calculated using collisionally excited lines, suggesting a possible correlation between low-abundance discrepancy factors and intermediate-period post-common-envelope central stars and/or Wolf-Rayet central stars. The detection of a radial velocity variability associated with the binarity of the central star of IC 4776 may be indicative of a significant population of (intermediate-period) post-common-envelope binary central stars that would be undetected by classic photometric monitoring techniques.

Key words: binaries: spectroscopic – stars: mass-loss – ISM: jets and outflows – planetary nebulae: individual: (IC 4776, PN G002.0−13.4).

1 INTRODUCTION

Planetary nebulae (PNe) are the intricate, glowing shells of gas ejected by low- and intermediate- mass stars at the end of their asymptotic giant branch (AGB) evolution which are then ionized by the emerging pre-white dwarf core. With some ∼80 per cent of all PNe showing deviation from spherical symmetry (Parker et al. 2006), it has proven impossible to understand their structures in terms of single star evolution (Soker 2006; Nordhaus, Blackman & Frank 2007; García-Segura et al. 2014), with binarity frequently invoked to explain their diverse, often strongly axisymmetrical morphologies (De Marco 2009; Jones & Boffin 2017).

Whilst a lower limit to the close-binary central star fraction is well constrained (at ∼20 per cent) by photometric monitoring surveys (Miszalski et al. 2009a), it is insufficient to explain all aspherical PNe. The remaining aspherical PNe are generally understood to be the products of mergers, wider binaries and/or weaker binary interactions (i.e. the engulfment of a Jovian mass planet; De Marco & Soker 2011). This hypothesis is supported by common-envelope (CE) population synthesis models, which predict a significant number of post-CE binaries with orbital periods of several days to a few weeks (e.g. Han, Podsiadlowski & Eggleton 1995) whilst almost all of the known post-CE central stars have periods less than 1 d (Jones & Boffin 2017).

The lack of known post-CE central stars with intermediate periods (only three are known to have periods greater than 3 d, Méndez & Niemela 1981; Manick, Miszalski & McBride 2015; Miszalski et al. 2017) is, perhaps, not unreasonable given that the amount

★ E-mail: paula@camk.edu.pl

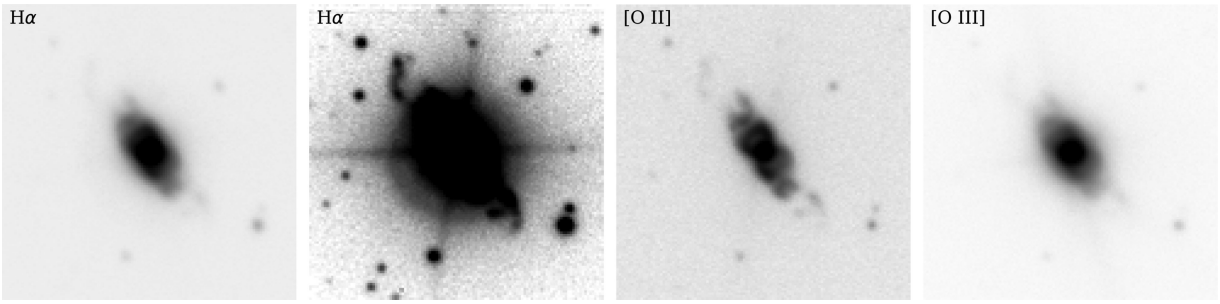

Figure 1. FORS2 narrowband imagery of IC 4776. Both Hα images include the light of [N II], and the central region of the rightmost Hα image is heavily saturated but most clearly shows the structure of the faint, precessing jets. All images measure $0.5' \times 0.5'$, north is up and east is left.

of the effort has been focused on photometric monitoring that becomes particularly insensitive at these longer periods (De Marco, Hillwig & Smith 2008; Jones & Boffin 2017). Recent work, however, has shown that targeted radial velocity monitoring can begin to reveal these missing binary systems (Miszalski et al. 2017; Jones et al. 2017). Constraining this population is of particular interest given that observations of 'naked' (i.e. those with no surrounding PN) white dwarf plus main-sequence binaries find a similar dearth of intermediate-period systems (Nebot Gómez-Morán et al. 2011), strongly indicating that the lack of known systems is not purely an observational bias. Understanding to what extent this population is truly absent (rather than just difficult to detect) will greatly further our understanding of the CE process itself (Toonen & Nelemans 2013).

IC 4776 is a relatively bright, small planetary nebula comprising a central, bipolar, hourglass-like structure and an extended, jet-like structure revealed for the first time by the images presented in this paper (see Fig. 1 and Section 2.1). Both jets and hourglass structures have been strongly linked to binary central stars (Miszalski et al. 2009b). The nebula has been shown to display dual-dust chemistry (i.e. features associated with both carbon- and oxygen-rich dust; Perea-Calderón et al. 2009; Górny et al. 2010), which has also been linked to a possible binary evolution of the nebular progenitor (Guzman-Ramirez et al. 2014). The spectral type of its central star is unclear but has been classified by various authors as [WC] (e.g. Aller & Keyes 1985). The apparent presence of narrow emission lines has also considered it as a *wels* classification (Tylenda, Acker & Stenholm 1993), now generally not considered as a valid classification given that in many cases the emission lines themselves do not originate from the stars but from their host nebulae (Basurah et al. 2016) or are the product of the irradiation of a main-sequence companion (Miszalski et al. 2011b).

Based on the likelihood that it hosts a binary central star, IC 4776 was selected for further study as part of a programme to search for binary central stars through time-resolved radial velocity monitoring. Here, we present the results of that radial velocity study, revealing variability consistent with an intermediate-period, post-CE binary. We furthermore present spatio-kinematic and chemical analyses of the nebula itself, in order to further constrain the relationship between the nebula and the probable central binary.

2 NEBULAR MORPHOLOGY AND KINEMATICS

2.1 FORS2 narrowband imagery

Narrowband imagery of IC 4776 was obtained using the FORS2 instrument mounted on ESO's VLT-UT1 (Appenzeller et al. 1998). Exposures were acquired in the following emission lines: Hα+[N II] (5 s exposure time on 2012 September 5 and 30 s on 2016 June 11), [O II] λ3727 (20 s on 2012 September 3) and [O III] λ5007 (5 s on 2012 September 5). In each case, the seeing was better than 1 arcsec. The de-biased and flat-fielded images are presented in Fig. 1.

In all three bands, the nebula shows a similar morphology, namely an 'X'-shape, which is most prominently visible in the light of [O II] λ3727. At all three wavelengths the central shell appears the brightest, whilst only at [O II] λ3727 it is possible to discern its detailed structure. This hourglass morphology is extremely similar to that of MyCn 18, a PN often hypothesized to have originated from a binary interaction owing to its similarity to some nebulae surrounding symbiotic binary stars (Corradi & Schwarz 1993). MyCn 18, in addition to its central hourglass, displays a system of high-velocity knots that may well be analogous to the jets observed in IC 4776 (Bryce et al. 1997; O'Connor et al. 2000), further highlighting the similarities between the two nebulae. The jets of IC 4776 are evident in all filters but most prominently in the light of Hα where their remarkable structure is clearest. The evident curvature of the jets is a strong indication of precession, which can be a natural product of a central binary system (Raga et al. 2009). Such precessing jets have been observed in several close-binary PNe, e.g. Fg 1 (Boffin et al. 2012), ETHOS 1 (Miszalski et al. 2011a) and NGC 6337 (García-Díaz et al. 2009; Hillwig et al. 2016), providing a solid observational link between jets and binarity.

2.2 FLAMES-GIRAFFE integral field spectroscopy

Spatially resolved, high-resolution, integral-field spectroscopy of IC 4776 was obtained on 2013 August 8 using FLAMES-GIRAFFE mounted on ESO's VLT-UT2 (Pasquini et al. 2002). The seeing during the observations did not exceed 1 arcsec. The ARGUS integral field unit, employed in its standard '1:1' scale mode (resulting in a total aperture of 11.5 × 7.3 arcsec sampled by an array of 22 × 14 0.52× 0.52 arcsec^2 microlenses), was used to feed the GIRAFFE spectrograph set-up with the H665.0/HR15 grating (providing a resolution of $R \sim 30\,000$ in the range 6470 Å $\lesssim \lambda \lesssim$ 6790 Å). ARGUS was oriented at P.A. $= 38^\circ$ (to coincide with the symmetry axis of the nebula) and with only two telescope pointings, offset by about 10 arcsec to each other, we were able to obtain a complete coverage of the nebula (which is ∼20 arcsec long including the faint extended emission), as shown in Fig. 2. Two exposures of 245 s were obtained for each of the two pointings, with the resulting data reduced and combined to produce a single, wavelength-calibrated data cube for each pointing using the standard ESO-GIRAFFE pipeline. Finally, the data from the two pointings were corrected to heliocentric velocity and combined to form a single data cube using specially written PYTHON routines.

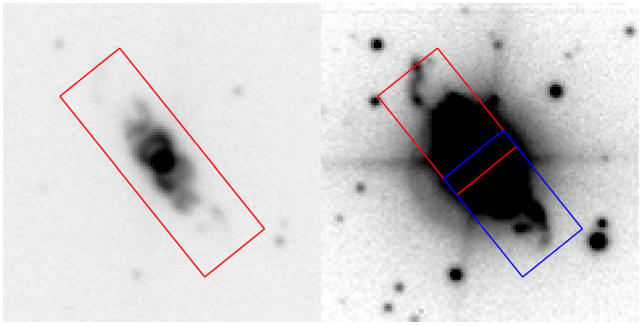

Figure 2. The ARGUS-IFU coverage of IC 4776. Each image measures 1×1 arcmin^2. North is up, and east to the left. Left: the two pointings merged together, overplotted on the FORS2 image in the light of [O II]. Right: the two pointings shown separately, overplotted on the FORS2 image in the light of Hα in order to highlight the spatial coverage of the jets.

In the wavelength range of the ARGUS data there are several spectral lines: Hα, [N II] $\lambda\lambda$6548,6584 and the [S II] $\lambda\lambda$6717,6731 doublet. In order to probe the kinematics and the morphology of the nebula, we focus on the [N II] λ6584 line given that it is brighter than [S II] $\lambda\lambda$6717,6731 and has a lower thermal width than Hα.

Channel maps for the [N II] λ6584 line are shown in Fig. 3. Each channel shows a cross-section through the nebula at a different velocity relative to the rest velocity of [N II] λ6584, starting from the top left-hand side channel being the most blueshifted (velocity of about -130 km s^{-1}), ending on the bottom right-hand side channel being the most redshifted (velocity of about 137 km s^{-1}). Each channel is a sum of three slices of the reduced cube where the wavelength step between slices is approximately 0.05 Å (i.e. each channel represents a range of 0.15 Å $\equiv$ 6.83 km s^{-1} at [N II] λ6584). The brightness/contrast is calculated individually for each

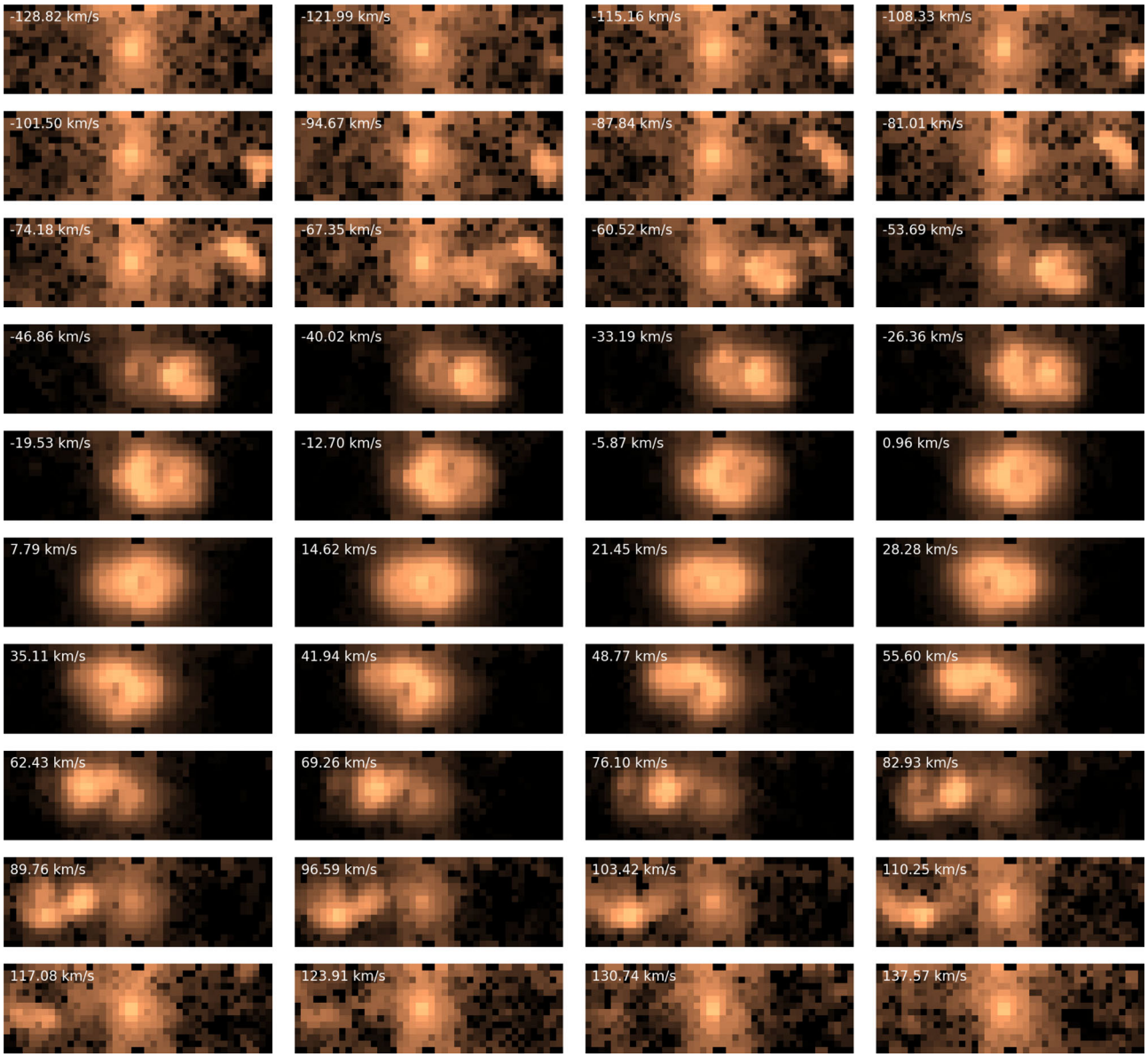

Figure 3. Velocity channel map for the [N II] λ6583.45 emission from IC 4776. Velocities are corrected to heliocentric velocity, and each channel represents the summed emission of three 'slices' of the reduced data cube, corresponding to a velocity bin of 6.83 km s^{-1}. The logarithmic display limits for each channel are calculated individually in order to maximize the features visible on each map.

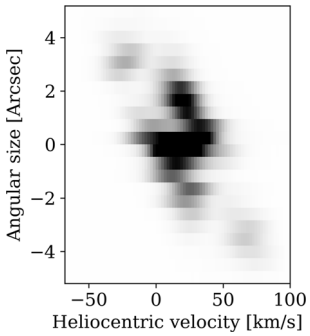

Figure 4. Simulated position velocity corresponding to an [N II] λ6583.45 Å longslit, with width ∼1 arcsec, placed along the symmetry axis of the nebula.

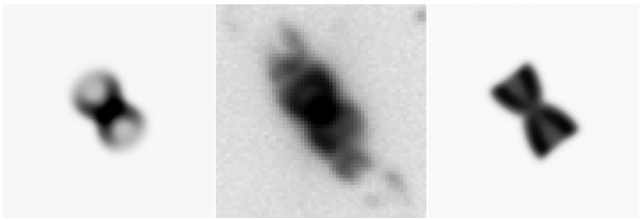

Figure 5. Synthetic images of the SHAPE model of IC 4776 at the derived inclination of 42° (left) and at an inclination of 90° (right). The central image is the FORS2 [O II] image (reproduced from Fig. 1 for direct comparison). Each image measures 0.25 × 0.25 arcmin^2.

channel using a logarithmic function in order to display the maximum amount of structural information possible.

The systemic velocity of the nebula has been previously found to be $v_{sys} = 16.3 \pm 0.6$ km s^{-1} (Durand, Acker & Zijlstra 1998), and around this velocity the channel maps present two circular structures joined at the position of the central star. This can be interpreted as the contribution of the two lobes of an inclined bipolar shell, as inferred from the imagery presented in Section 2. Further from this central velocity, one lobe begins to dominate, just as would be expected from an inclined hourglass. Yet further still from the systemic velocity (e.g. $v_{sys} \pm \sim$20 km s^{-1}), a second component begins to contribute significantly to the observed emission in each channel map, initially appearing close to the central star and then moving away at velocities furthest from the systemic velocity. This emission feature clearly originates from the jets, presenting with a similarly curved appearance at the largest velocities. The jets themselves also present clearly greater velocities than the central shell (the maximum extent of which is at roughly $v_{sys} \pm 35$ km s^{-1}), reaching more than 100 km s^{-1} away from the systemic velocity. Furthermore, there is an evident asymmetry in the jet velocities given that the blueshifted jet reaches roughly $v_{sys} - 130$ km s^{-1}, whilst the redshifted component only reaches as far as $v_{sys} + 100$ km s^{-1}. Fig. 2 reinforces this idea as in the high-contrast image the Northern jet extends beyond the region encompassed by the FLAMES-GIRAFFE observations (centred on the central star), whilst the Southern jet is apparently well covered. Given the clear precession visible in both the imagery and IFU spectroscopy it is not possible to derive a simple correlation between line-of-sight velocity and distance from the central star which would further constrain the asymmetry.

A 2 spaxel region surrounding the central star was collapsed (equivalent to a slit-width of 1.04 arcmin) in order to produce a simulated longslit spectrum. The position–velocity array of this simulated longslit is shown in Fig. 4. The position–velocity array shows a clear 'X'-shape, typical of such bipolar, hourglass structures, as well as end-caps corresponding to the brightest regions of jet emission (further emission from the jets can be seen with increased contrast that blows out the central nebula).

2.3 Shape modelling

A spatio-kinematic model of the central hourglass of IC 4776 was constructed based on the narrowband imagery and spatially resolved spectroscopy presented above. The SHAPE software was used, following the standard workflow presented in Steffen et al. (2011), varying both morphological and kinematic parameters over a wide range of parameter space with the best fit being determined from a by-eye comparison of synthetic images and velocity channel maps to the observations. The jets themselves are too complex to be treated by a simple spatio-kinematic model, and their detailed modelling is reserved for a subsequent paper (Santander-García et al., in preparation). Although, it is worth noting that, in principle, the data are of sufficient quality to derive the precession properties of the jets, which can then be related to the parameters of the central binary star (e.g. Raga et al. 2009; Boffin et al. 2012) at the time the jet was launched (constrained by the kinematical age of the jet).

The best-fitting SHAPE model, as expected from the appearance of the nebula in the narrowband imagery, comprises an hourglass-like structure whose symmetry axis is inclined at 42° ± 4° with respect to the plane of the sky (see Fig. 5). The velocity structure of the nebula is found to be well represented by a flow law whereby all velocities are radial from the central star and proportional to the distance from the central star. Such flow laws, often referred to as 'Hubble flows', are generally taken to imply an eruptive event in which the majority of the nebular shaping occurred during a brief time period. However, Steffen, García-Segura & Koning (2009) showed that whilst deviations from a 'Hubble flow' should be appreciable and easily observed in PNe formed via the classical interacting stellar winds model (Kwok, Purton & Fitzgerald 1978; Kahn & West 1985), such a simple flow law will provide a good first-order estimation of the overall morphological and kinematic properties of the nebula. Particularly given the relatively low spatial resolution of the FLAMES-GIRAFFE observations cf. the size of IC 4776, we are unable to constrain the presence (or absence) of such deviations from a 'Hubble flow'.

The systemic velocity of the nebula is found to agree well with the literature value of 16.3 ± 0.6 km s^{-1} (Durand et al. 1998) and was fixed in the modelling. The kinematical age of the nebula is found to be approximately 300 yr kpc^{-1} (with a significant uncertainty due to the small size of the nebula). Whilst there is significant variation in distance determinations for IC 4776 in the literature, the kinematical age would imply a rather young nebula at all but the very largest distances. The distance of 1.01 kpc determined by Phillips & Pottasch (1984) would seem to imply an impossibly young nebula, whilst the distances derived by Stanghellini, Shaw & Villaver (2008, 4.97 kpc) and Frew, Parker & Bojičić (2016, 4.44 ± 1.27 kpc) would give a more reasonable age of ∼1500 yr.

3 NEBULAR CHEMISTRY

High-resolution longslit spectroscopy of the nebula IC 4776 was acquired on 2016 August 9 using the Ultra-violet and Visual Echelle Spectrograph (UVES) mounted on ESO's VLT-UT2 (Dekker et al. 2000). Exposures were acquired using both arms of the spectrograph with the following set-ups. Using Dichroic 1

(3 × 150 s exposures, 1 × 20 s exposure), the blue arm was set to a central wavelength of 3460 Å (with the standard HER_5 blocking filter) whilst the red arm was set to a central wavelength of 5800 Å (with the standard SHP700 blocking filter). Using Dichroic 2 (3 × 300 s exposures, 1 × 60 s exposure, 1 × 20 s exposure), the blue arm was set to a central wavelength of 4370 Å (again with the standard HER_5 blocking filter) whilst the red arm was set to 8600 Å (with the standard OG590 blocking filter). A slit-width of 2.4 arcsec was employed, and the seeing during the observations was approximately 1.5 arcsec. The spectra were reduced using the standard UVES pipeline and flux-calibrated using 300 s exposures of the standard star LTT 7987 taken with the same set-ups directly following the observations of IC 4776. Collectively, the spectra provide near-continuous wavelength coverage from ∼3000 to 10 000 Å (see Fig. A1). To construct the final spectrum, we took the median of the flux at each wavelength from the longest exposures in each set-up, and where lines were saturated, replaced the affected ranges with values from the shorter exposures in which saturation was not an issue.

Emission line fluxes were measured using the ALFA code (Wesson 2016), which optimizes parameter fits to the line profiles using a genetic algorithm following the subtraction of a global continuum. The effectiveness of ALFA in measuring PN line fluxes has previously been demonstrated in several papers (e.g. Jones et al. 2016), and is further demonstrated in Figs 7 and A1. ALFA assumes that all lines have a Gaussian profile. At the high resolution of the UVES spectra, velocity structure is evident, and lines of different ionization have different profiles. For the purposes of chemical analysis, we binned the spectra by a factor of 10 in wavelength, resulting in Gaussian profiles for all lines.

353 emission lines were measured, of which 329 were resolved and 24 were blends of 2 or more lines. Échelle spectra may contain many spurious features due to bleeding of strong lines from adjacent orders. In general, these do not affect the analysis, as ALFA only attempts to fit features close to the wavelengths of known emission lines. Spurious features not fitted by ALFA may be seen in panels (a) and (b) of Fig. 7 (though they are also present in all panels of Fig. A1). However, in a few cases, the bleeding may be blended with nebular emission. The O II recombination line (ORL) at 4089 Å is one such case, and this impacts the estimate of the temperature and density from the ratios of O II lines, as discussed below. Table A1 lists the observed and dereddened fluxes measured for all emission lines measured in the spectra, together with their 1σ uncertainties.

Physical conditions as well as chemical abundances were calculated from the emission line fluxes using the NEAT code (Wesson, Stock & Scicluna 2012). The code uses Monte Carlo techniques to propagate uncertainties in line flux measurements into the derived quantities (for full details, see Wesson et al. 2012). The physical parameters determined for IC 4776 are listed in Table 1.

The extinction towards the nebula was estimated from the flux-weighted average of the ratios of Hα, Hγ and Hδ to Hβ, and the Galactic extinction law of Howarth (1983). Hγ and Hδ are in the same spectrum as Hβ, whilst Hα is in a separate spectrum. The three lines give consistent estimates of the logarithmic extinction at Hβ, c(Hβ), which is 0.22 ± 0.03.

The nebular density is estimated using several standard collisionally excited line (CEL) diagnostics, as well as from the Balmer and Paschen decrements, and the ratios of O II ORLs. The CEL diagnostics give relatively high densities of 10 000–30 000 cm^{-3}; the Paschen and Balmer decrements also imply high densities, of 10^4–10^5 cm^{-3}, although with larger uncertainties (see Fig. 6). The O II ORL ratios imply a lower density of ∼3000 cm^{-3}, with the caveat that the 4089 Å line flux on which the ratios rely may be overestimated due to bleeding from adjacent orders. If its flux is overestimated, the density derived is underestimated.

Table 1. Extinction, temperatures and densities of IC 4776 as derived using the NEAT code, as well as the temperatures and densities used for the determination of the chemical abundances are listed in Tables 2 and 3.

c(Hβ) =	0.22	± 0.03
n_e([O II]) (cm^{-3}) =	9660	$^{+10020}_{-3610}$
n_e([S II]) (cm^{-3}) =	11 600	$^{+9000}_{-3600}$
n_e([Cl III]) (cm^{-3}) =	18 600	$^{+5500}_{-3900}$
n_e([Ar IV]) (cm^{-3}) =	41 300	$^{+4500}_{-4000}$
n_e(BJ) (cm^{-3}) =	11 400	$^{+16900}_{-6800}$
n_e(PJ) (cm^{-3}) =	57 500	$^{+54500}_{-28000}$
T_e([O II]) (K) =	30 800	$^{+4200}_{-16800}$
T_e([S II]) (K) =	18 000	$^{+17000}_{-9300}$
T_e([N II]) (K) =	12 000	$^{+1000}_{-1200}$
T_e([O III]) (K) =	10 000	± 200
T_e([Ar III]) (K) =	9070	± 180
T_e([S III]) (K) =	11 100	± 400
T_e(BJ) (K) =	8920	$^{+760}_{-700}$
T_e(PJ) (K) =	7240	$^{+1070}_{-940}$
T_e(He 5876/4471) (K) =	3180	$^{+1060}_{-800}$
T_e(He 6678/4471) (K) =	3970	$^{+1710}_{-1190}$
T_e(O II ORLs) (K) =	3560	$^{+3710}_{-1960}$
n_e(O II ORLs) (cm^{-3}) =	2850	$^{+1430}_{-1240}$

Temperatures determined from CEL ratios are around 10 kK. The Balmer and Paschen jumps are well detected and permit the derivation of temperatures from their magnitudes. They are statistically consistent with each other, but slightly lower than the temperatures from CELs, with T(BJ) = 8900 ± 800 K, and T(PJ) = 7200 ± 1000 K, where T([O III]) = 10000 ± 200 K. The ratios of the three strong helium lines at 4471, 5876 and 6678 Å are weakly temperature sensitive, and these are well enough detected to enable their use as a diagnostic; the temperatures from the λ5876/λ4471 and the λ6678/λ4471 ratios are significantly lower than from other aforementioned methods, at 3–4 kK. Finally, O II ORL ratios imply a temperature consistent with the helium line ratios, albeit with a large statistical uncertainty, in addition to the systematic uncertainty of the effect of bleeding, which would result in an underestimate of the temperature.

Chemical abundances were derived from both CELs and ORLs with total chemical abundances derived using the ionization correction scheme of Delgado-Inglada, Morisset & Stasińska (2014). Heavy element ORLs are very well detected in the spectra, and as such it is possible to measure abundances for C^{2+}, C^{3+}, O^{2+}, N^{2+}, N^{3+} and Ne^{2+}. The NEAT code employed for the analysis assumes a three-zone ionization scheme. The average of n_e([O II]) and n_e([S II]) was adopted as a representative of the density of low-ionization zone (Ionization Potential, IP < 20 eV), whilst the average of n_e([Cl III]) and n_e([Ar IV]) was applied for the medium ionization zone (20 eV < IP < 45 eV). The electron temperature obtained from [N II] was used as the temperature of the low-ionization zone, and the average of the temperatures derived using [O III], [Ar III] and [S III] lines is taken as

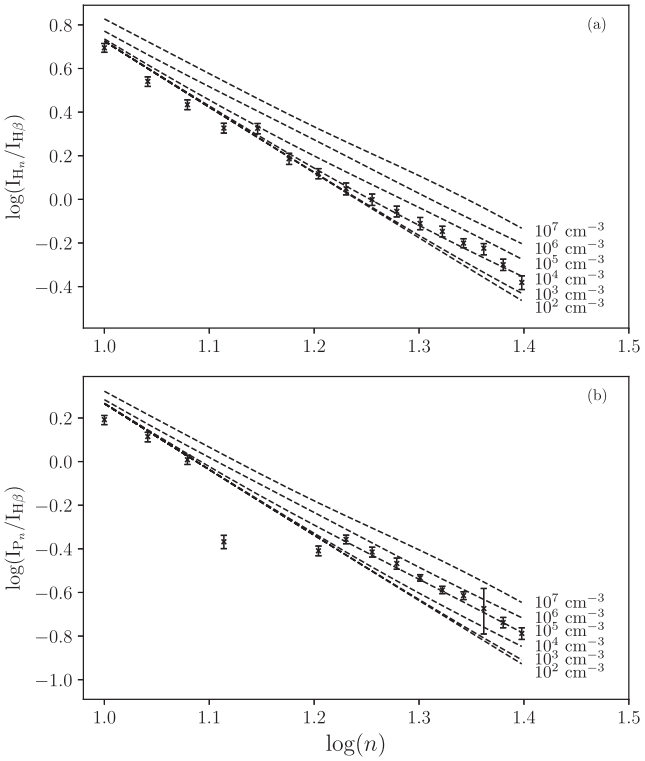

Figure 6. Observed intensities (relative to H $\beta = 100$) of high-order Balmer (a) and Paschen (b) lines as a function of the principal quantum number n. The dashed curves show the predicted intensities of the lines as a function of electron density, at a temperature of 10 000 K as derived from the [O III] nebular to auroral line ratio. The plots highlight the general tendency towards larger densities ($\sim 10^4$–10^5 cm^{-3}), consistent with those measured from CEL diagnostics. Note that H14 is blended with a line of [S III] and, as such, its flux is overestimated. P13 and P16 lie close to the ends of two of our spectra where the flux calibration uncertainties are large (and not reflected in the plotted uncertainties which are simply the statistical uncertainties on the flux measurement), and as such their fluxes are almost certainly underestimated given that they fall well below the trend of the other measured lines. P14 and P15 are not shown as they lie in a gap in our spectral coverage.

the temperature of the medium-ionization zone. No lines of the high-ionization regime (IP > 45 eV) are detected, so no high-ionization conditions are assumed. The medium-ionization parameters were also employed in the derivation of abundances from ORLs. The calculated abundances, from both ORLs and CELs, are listed in Tables 2 and 3.

O^{2+} permits the best determination of the abundance discrepancy, as ORLs and CELs of the ion are both present in optical spectra. 68 O II ORLs are detected, together with the 3 strong [O III] CELs at 4363, 4959 and 5007 Å. The abundances derived from the well-detected multiplets V1, V2, V10, V12 and V19 agree very well with each other; lines from multiplets V5, V20, V25, V28 and a number of 3d–4f transitions are detected, but imply much higher abundances and may be affected by noise or bleeding from strong lines in adjacent orders. As such, the total O^{2+} abundance is derived based only on the five well-detected multiplets. The abundance for each multiplet was determined from a flux-weighted average of the detected components, and the overall abundance calculated as the average of the multiplet abundances. The O^{2+}/H^+ abundance thus derived is $(6.0 \pm 0.3) \times 10^{-4}$, whilst that derived from the strong CELs is $(3.4 \pm 0.2) \times 10^{-4}$, giving an abundance discrepancy factor (adf; the ratio of ORL abundance to CEL abundance) of 1.75 ± 0.15.

In the case of oxygen, for O^{2+} ORLs and CELs were detected whilst for O^+ only CELs were detected. The He^{2+}/H^+ ratio implies that there should be negligible O^{3+}, and so the CEL total abundance is simply the sum of O^+ and O^{2+}. For ORLs, it was assumed that the ionization structure is the same, and that the O^+/O ratio from CELs can be used to correct for it. Thus, the abundance discrepancy factors for O^{2+} and O are the same.

Lines of Ne^{2+} from both recombination and collisional excitation were also detected in the spectra. The ORLs give abundances consistent with each other, yielding a value of $(1.7 \pm 0.2) \times 10^{-4}$. The CELs give $(0.9 \pm 0.05) \times 10^{-4}$, resulting in a discrepancy factor of 1.9 ± 0.3, consistent with that derived for O^{2+}.

Optical spectra contain CELs only of N^+, but ORLs of both N^{2+} and N^{3+}. Most of the N is in the form of N^{2+}, and so the comparison of abundances relies on the large and uncertain correction of the CEL abundance for the unseen ions. Delgado-Inglada et al. (2014) proposed a new ICF scheme to compute N abundances; however, the differences with the classical ICF approach (N/O = N^+/O^+) can be very large, especially for relatively low-excitation PNe, as is the case of IC 4776. Using the newer ICF scheme, we obtain $N/H = 1.67 \times 10^{-4}{}^{+3.00\times10^{-5}}_{-3.60\times10^{-5}}$, whilst the classical approach gives an N abundance ∼0.4 dex lower. Delgado-Inglada et al. (2015) found that the Delgado-Inglada et al. (2014) ICF for N showed a correlation with both He abundance and degree of ionization and, as such, favoured the classical approach. As the ICF for N from Delgado-Inglada et al. (2014) is strongly dependent on whether the PN is radiation or matter bounded (providing a more realistic correction for matter-bounded PNe; Delgado-Inglada, private communication), we used the classical ICF approach to derive N abundances for IC 4776. The derived abundance discrepancy factor for N is 2.9, with statistical uncertainties of $^{+0.7}_{-0.4}$, though with systematic uncertainties it is probably much larger (especially given the uncertainty is the choice of ICF). The net result is that, whatever ICF we choose, the N/O ratio is relatively low ($-0.75 <$ log (N/O) < -0.35).

Without UV spectra, we cannot derive an abundance discrepancy factor for carbon. However, studies have generally found that ionic and elemental ratios from ORLs are consistent with those derived from CELs (Wang & Liu 2007; Delgado-Inglada & Rodríguez 2014). The C/O ratio derived from ORLs is 0.3, atypically low for a planetary nebula (which normally present values around unity[1]).

Very recently, Juan de Dios & Rodríguez (2017) have demonstrated the critical role of atomic data uncertainties in the determination of chemical abundances. They showed that the transition probabilities of the commonly used density diagnostic lines of S^+, O^+, Cl^{2+} and Ar^{3+} as well as the collision strengths of Ar^{3+} are responsible for most of the uncertainties in the derived total abundances, especially in the high-density (log (n_e) > 4.0) regime. Given that the computed density for IC 4776 is relatively high, especially for the medium ionization zone, it is important to note that the uncertainties derived for the total nebular abundances are almost certainly underestimated. However, the consistency between the adfs derived for O^{2+} and Ne^{2+} provides a strong indication of the validity of the results.

[1] Wesson, Liu & Barlow (2005) found an average C/O ratio of 0.85 in a sample of nebulae outside the solar circle, whilst Kingsburgh & Barlow (1994) find a value of 1.15 in a sample interior to the solar circle – both measured from CELs.

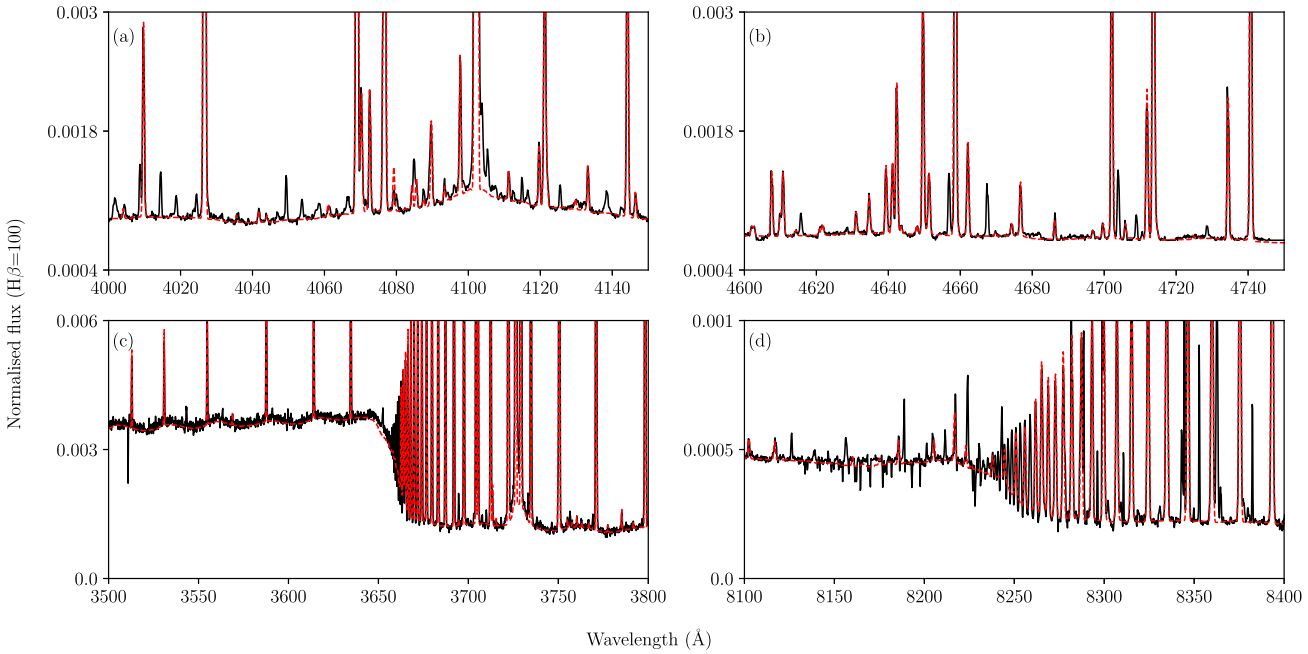

Figure 7. The ALFA spectral fit (red-dashed) overlaid on top of the combined, observed UVES spectra (black-solid). The panels highlight key regions used in the NEAT analysis: (a) and (b) show two regions containing O II ORLs critical for deriving the nebular adf, whilst the panels (c) and (d) cover the Balmer and Paschen jumps, respectively. The full spectrum is shown in Fig. A1.

Table 2. Ionic abundance ratios, by number, relative to H^+, in IC 4776.

Ion	$\frac{X^{i+}}{H^+}$	
He^+ (ORLs)	0.10	$\pm 2.00 \times 10^{-3}$
He^{2+} (ORLs)	1.68×10^{-5}	$^{+4.90\times10^{-6}}_{-4.80\times10^{-6}}$
C^0 (CELs)	9.49×10^{-9}	$^{+7.73\times10^{-9}}_{-3.40\times10^{-9}}$
C^{2+} (ORLs)	1.62×10^{-4}	$\pm 3.00 \times 10^{-6}$
C^{3+} (ORLs)	5.46×10^{-6}	$\pm 9.70 \times 10^{-7}$
N^+ (CELs)	3.91×10^{-6}	$^{+1.72\times10^{-6}}_{-8.70\times10^{-7}}$
N^{2+} (ORLs)	1.75×10^{-4}	$\pm 1.10 \times 10^{-5}$
N^{3+} (ORLs)	1.07×10^{-5}	$\pm 6.00 \times 10^{-7}$
O^+ (CELs)	2.22×10^{-5}	$^{+1.77\times10^{-5}}_{-6.80\times10^{-6}}$
O^{2+} (ORLs)	6.04×10^{-4}	$^{+3.20\times10^{-5}}_{-3.00\times10^{-5}}$
O^{2+} (CELs)	3.44×10^{-4}	$^{+2.20\times10^{-5}}_{-2.00\times10^{-5}}$
adf (O^{2+})	1.75	$^{+0.15}_{-0.14}$
Ne^{2+} (ORLs)	1.71×10^{-4}	$^{+2.20\times10^{-5}}_{-1.90\times10^{-5}}$
Ne^{2+} (CELs)	8.91×10^{-5}	$^{+5.70\times10^{-6}}_{-5.30\times10^{-6}}$
adf (Ne^{2+})	1.92	$^{+0.28}_{-0.24}$
Ar^{2+} (CELs)	1.34×10^{-6}	$^{+1.00\times10^{-7}}_{-9.00\times10^{-8}}$
Ar^{3+} (CELs)	1.15×10^{-7}	$^{+8.00\times10^{-9}}_{-7.00\times10^{-9}}$
S^+ (CELs)	2.60×10^{-7}	$^{+1.55\times10^{-7}}_{-5.80\times10^{-8}}$
S^{2+} (CELs)	3.65×10^{-6}	$^{+2.90\times10^{-7}}_{-2.70\times10^{-7}}$
Cl^+ (CELs)	3.36×10^{-9}	$^{+1.09\times10^{-9}}_{-7.70\times10^{-10}}$
Cl^{2+} (CELs)	8.48×10^{-8}	$^{+6.80\times10^{-9}}_{-6.30\times10^{-9}}$
Cl^{3+} (CELs)	1.54×10^{-8}	$^{+1.10\times10^{-9}}_{-1.00\times10^{-9}}$

Table 3. Total nebular abundances, relative to H, in IC 4776.

Element	$\frac{X}{H}$	
He (ORLs)	0.10	$\pm 2.00 \times 10^{-3}$
C (ORLs)	1.94×10^{-4}	$\pm 4.00 \times 10^{-6}$
N (ORLs)	1.85×10^{-4}	$\pm 1.10 \times 10^{-5}$
N (CELs)	6.38×10^{-5}	$^{+9.80\times10^{-6}}_{-1.24\times10^{-5}}$
adf (N)	2.92	$^{+0.73}_{-0.43}$
O (ORLs)	6.50×10^{-4}	$^{+5.10\times10^{-5}}_{-3.80\times10^{-5}}$
O (CELs)	3.71×10^{-4}	$^{+3.20\times10^{-5}}_{-2.40\times10^{-5}}$
adf (O)	1.75	$^{+0.15}_{-0.14}$
Ne (ORLs)	1.87×10^{-4}	$^{+2.70\times10^{-5}}_{-2.30\times10^{-5}}$
Ne (CELs)	1.04×10^{-4}	$^{+9.00\times10^{-6}}_{-7.00\times10^{-6}}$
adf (Ne)	1.77	$^{+0.26}_{-0.23}$
Ar (CELs)	2.05×10^{-6}	$^{+1.80\times10^{-7}}_{-2.30\times10^{-7}}$
S (CELs)	6.73×10^{-6}	$^{+9.90\times10^{-7}}_{-8.60\times10^{-7}}$
Cl (CELs)	1.04×10^{-7}	$^{+8.00\times10^{-9}}_{-7.00\times10^{-9}}$

4 CENTRAL STAR

4.1 Observations and data reduction

The central star of IC 4776 was observed a total of 10 times using the FORS2 instrument mounted on ESO's VLT-UT1 (Appenzeller et al. 1998). 1200 s exposures were acquired in the service mode, randomly distributed throughout the observing period (see Table 4 for the exact dates). For each observation, the same instrumental set-up was used, employing a longslit of width 0.5 arcsec and the GRIS_1200B grism resulting in a spectral range of 3700 Å $\lesssim \lambda \lesssim$ 5100 Å with a spectral resolution of approximately 0.8 Å.

Table 4. Radial velocities of the central star of IC 4776 with respect to the nebular systemic velocity.

Heliocentric Julian Date (days)	Radial velocity (km s^{-1})	
2456428.84873	−20.53	± 1.80
2456444.70375	49.28	± 3.66
2456445.75583	17.03	± 5.28
2456447.81343	−4.98	± 1.42
2456460.80640	16.01	± 2.08
2456460.82896	26.72	± 4.59
2456486.59737	−11.03	± 4.61
2456508.64040	47.42	± 7.44
2456531.59275	−30.92	± 1.68
2456564.53724	−18.70	± 2.37

All data were bias subtracted, wavelength calibrated and optimally extracted using standard STARLINK routines (Shortridge et al. 2004).

4.2 Radial velocity variability

After the reduction, the spectra were continuum subtracted and aligned using the He I λ4471.48 nebular line, such that the systemic nebular velocity was at 0 km s^{-1} (thus accounting for both heliocentric velocity variations between observations and small deviations in the wavelength calibration). The Balmer lines were all found to be severely contaminated by the bright surrounding nebula, essentially leaving only the absorption line of He II λ4541 as a 'clean' feature for cross-correlation. The individual spectra were all cross-correlated against a custom mask (namely a flat continuum with a deep, narrow absorption spike at the rest velocity of the He II feature) with the resulting radial velocities (cf. the nebular systemic velocity) listed in Table 4, and plotted in Fig. 8.

There is a clear variation in the radial velocity with a semi-amplitude of about 30–40 km s^{-1} strongly indicating that the central star of IC 4776 is a binary system. Unfortunately, with so few radial velocity points, it is not possible to fully constrain the orbital period of the likely binary, with several periodicities and amplitudes providing reasonable fits to the data. Our current radial velocity data rule out periods much longer than 20 d, but shorter periods are relatively well fit. In Fig. 8, we show a tentative fit with a period of 9 d to highlight the significant radial velocity variations most likely due to orbital motion, as well as the need for further data. Interestingly, although the stellar systemic velocity (the zero of the sine curve used to fit the stellar radial velocities, often referred to as γ) was allowed to vary as part of the fitting procedure, it was found to coincide with the systemic velocity of the nebula (at zero in the plot given that the all radial velocities have been measured with respect to the nebular systemic velocity) within uncertainties ($\Delta v = v_{\rm neb} - \gamma \sim 3$ km s^{-1}). This indicates that the plotted fit may indeed be close to the true orbital solution. However, it must be emphasized that we find similar good fits for a range of periods, including ∼0.3 and ∼1.2 d.

It is important to note that we do not see any clear signs of a secondary component in our spectra. Previous authors have classified the central star as a *wels* type (Tylenda et al. 1993) indicating that perhaps some emission lines attributable to the secondary could be present in the spectra. However, the extremely bright and compact nature of the central region of the nebula can account for the presence of these lines (Basurah et al. 2016). We find the same bright, narrow emission lines in our 2D spectra, but find no evidence of an appreciable contribution to their flux from the central star; rather, they originate purely from the compact nebula (although accurate nebular subtraction is a challenge). Assuming that no such stellar emission lines are present and that the secondary is a main-sequence star (the most common scenario; Jones & Boffin 2017), short periods (≤1 d) are unlikely given that at short periods a main-sequence star would be expected to show strong emission lines due to irradiation (Miszalski et al. 2011b; Jones et al. 2014, 2015). However, if the secondary is a fainter white dwarf, then short periods cannot be ruled out on the basis of the non-detection of irradiated lines in the spectrum.

Assuming that the nebular inclination derived in Section 2.3 is reflective of the inclination of the binary (as found in all cases where both inclinations are known; Hillwig et al. 2016), then it is possible to place some limits on the possible mass of the secondary. Further assuming that the amplitude of the fit shown in Fig. 8, $K_1 \sim 40$ km s^{-1}, is representative of the true amplitude (a seemingly reasonable assumption given the relatively even distribution of the radial velocity data points), then a 9 d period would imply a mass ratio ($q = \frac{M_2}{M_1}$) of around unity. Longer periods and/or greater radial velocity amplitudes would both imply higher mass ratios and vice versa. The mass function for the secondary can be written as

$$f(M_2) = \frac{M_2^3 \sin^3 i}{(M_1 + M_2)^2} = \frac{P K_1^3}{2\pi G}, \quad (1)$$

where M_1 and M_2 are the primary and secondary masses, i is the inclination of the orbital plane, and P is the orbital period.

Taking a relatively standard white dwarf mass for the primary of $M_1 = 0.6$ M$_\odot$ (and maintaining the assumption that $K_1 \sim 40$ km s^{-1}), the mass function can be solved analytically for the secondary mass. Taking into account the uncertainty on the nebular inclination (based on the spatiokinematical modelling presented in Section 2.3), the possible range of secondary masses are plotted as a function of period in Fig. 9. Under these assumptions, the tentative 9 d period would imply that the secondary is likely a late-type main sequence star (roughly of spectral type K) or a white dwarf. For the secondary to be a white dwarf, it would have to have been initially the more massive component of the binary and, as such, would be expected to leave a more massive remnant (at least more massive than the primary remnant which, in this case, was assumed to be 0.6 M$_\odot$). This is a possibility given that the open mass range for the secondary, based on our fits, is approximately 0.6–0.7 M$_\odot$. However, a more massive secondary would probably be required in order for it to have now cooled beyond observability in our spectra. If the true period is shorter than 9 d (Fig. 9 also shows solutions for the reasonable fits at 0.3 d and 1.2 d) and then the open mass range would be significantly lower, ruling out an evolved white dwarf companion for the same reason, whilst a main-sequence secondary would become less likely given the aforementioned non-detection of irradiated emission lines originating from the secondary. However, this effect may be counteracted by the implied low secondary masses (and therefore radii) at shorter periods, as the level of irradiation in such systems is principally a function of the apparent radius of the irradiated star (proportional to the ratio of the secondary radius and the orbital separation).

Greater radial velocity amplitudes than the assumed ∼40 km s^{-1} would open the possibility of a more massive white dwarf companion, but the currently available data provides no indication of such a large amplitude. Similarly, periods longer than 9 d open the parameter space to the possibility of a more massive, evolved white dwarf companion, however in that case the system would have to have undergone two CE phases (given that the AGB radius of a

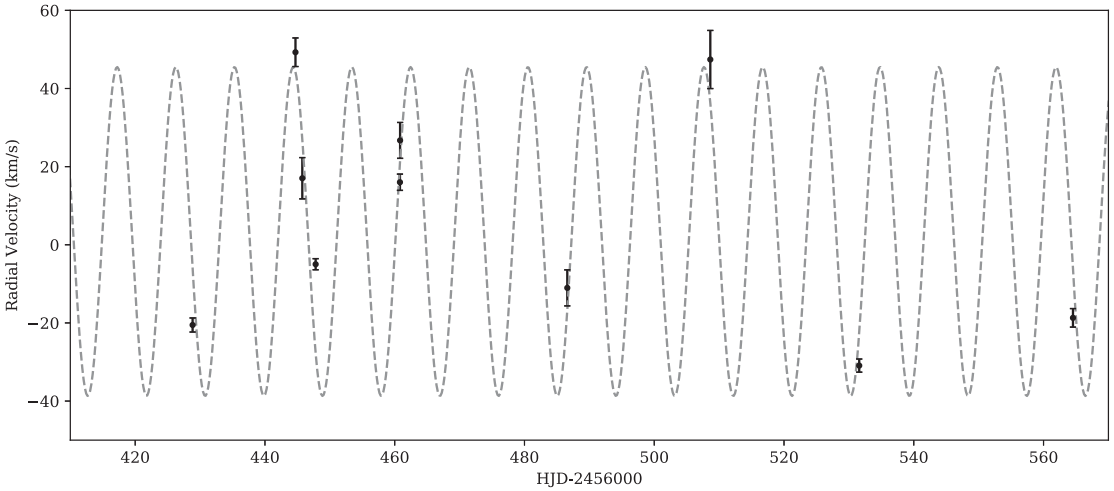

Figure 8. Radial velocity curve of the central star of IC 4776 based on the FORS2 data with a tentative fit of period equal to 9 d. It is important to note that similar good fits can be made with shorter periods, including periods around 0.3 and 1.2 d. Further observations are essential to fully constrain the period.

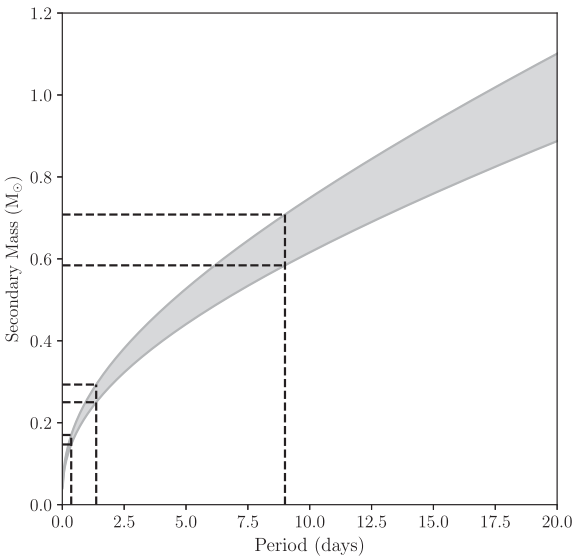

Figure 9. A plot showing the possible secondary masses of IC 4776 (shaded region) as a function of period for the FORS2 radial velocity data. The plot assumes the same radial velocity amplitude as the fit of Fig. 8 and a 0.6 $M_{\odot}$ primary in a circular orbit. The range of possible masses for a given period is derived assuming that the binary is coplanar with the waist of the nebula, and the range of values for a given period is a reflection of the uncertainty on the nebular inclination. The periods which offer similar good fits to the radial velocity data are delineated to highlight the approximate range of possible secondary masses (∼0.1–0.7 $M_{\odot}$) For more detail refer to the text.

more massive companion would inevitably have been larger than that of the primary) which almost certainly would result in a very short orbital period (Tovmassian et al. 2010). Therefore, on a stellar evolutionary basis, a main-sequence secondary (roughly of *K*-type for a period of 9 d, or late *M*-type for periods less than 1 d) would seem to be a more plausible companion, although a white dwarf secondary cannot be entirely ruled out.

5 DISCUSSION

Population synthesis models predict many post-CE systems with periods of several to a few tens of days (e.g. Han et al. 1995). However, the known population of post-CE binary central stars of PNe is very sparse in this region (De Marco et al. 2008; Jones & Boffin 2017), with a similar paucity observed in the general white dwarf plus main-sequence binary population (Nebot Gómez-Morán et al. 2011). Thus far, it is unclear whether this lack of intermediate-period binary central stars represents pure failure of the population synthesis models[2] or also an observational bias towards the discovery of short-period systems.

Recent observations have indicated that long-term radial velocity monitoring with modern, high-stability spectrographs may hold the key to revealing this missing intermediate-period population, should it indeed exist (e.g. Miszalski et al. 2017). Here, we have reported on the discovery of a post-CE binary star at the centre of IC 4776 via such radial velocity monitoring. Whilst the period of the system cannot be confirmed by the data (several periods ranging from ∼0.3–9 d provide reasonable orbital solutions), the detection further supports the hypothesis that a systematic radial velocity survey may indeed reveal the presence of many intermediate-period binaries inside PNe.

The central star of IC 4776 was found to be a single-lined binary with a tentative orbital period of ∼9 d (though shorter periods cannot be ruled out), where the secondary is most likely a main-sequence star (of mass ∼0.1–0.7 $M_{\odot}$). The system was selected for monitoring based primarily on the presence of precessing jets, believed to result from mass transfer in a central binary system. Such mass transfer has been hypothesized to occur either prior to or immediately after the CE phase (Corradi et al. 2011; Boffin et al. 2012; Miszalski, Boffin & Corradi 2013; Tocknell, De Marco & Wardle 2014), but may also help to prevent in-spiral during the CE as part of a grazing envelope evolution (GEE; Soker 2015; Shiber, Kashi & Soker 2017). Such a GEE may lead to the preferential formation of wide binaries, but the range of possible periods derived

[2] It is important to note that population synthesis models rely on an ad hoc prescription of the CE process, often relying on simple parametrizations that have been proven to be less than satisfactory in reproducing observations (De Marco et al. 2011). Hydrodynamic models thus far fall short of being able to make the predictions required for use in population synthesis (Ivanova et al. 2013), however tend to almost unanimously predict very short post-CE orbital periods whilst the few that do predict longer periods seem to be under-resolved (see e.g. Passy et al. 2012).

for IC 4776 does not extend to long enough periods to necessitate a GEE to explain its formation (though nor does it rule out such an evolution).

An empirical analysis of the chemical abundances in IC 4776 based on échelle spectra covering the entire optical range indicates a low N/O ratio as well as a low C/O ratio (both of which are ∼0.3). This may be indicative that interaction with the companion cut short the AGB evolution of the nebular progenitor (De Marco 2009; Jones et al. 2014).

In PNe, there is a long-standing discrepancy between chemical abundances derived using ORLs and those derived using CELs, which has often been attributed to the existence of a second phase of cold-hydrogen-deficient material within the normal nebular gas phase (Liu et al. 2000; Tsamis et al. 2003; Zhang et al. 2004; Wesson et al. 2005). The discrepancy is typically a factor of 2–3 but exceeds a factor of 5 in about 20 per cent of nebulae. Recent observations have suggested that high-abundance discrepancies may be strongly correlated with central stars that have undergone a CE evolution (Corradi et al. 2015; Jones et al. 2016; Wesson et al. 2017). However, our chemical analysis reveals the adf of IC 4776 to be particularly low at ∼2, which is not just low for a PN with a binary central star, but for PNe in general. Interestingly, the only other post-CE system known to reside in a low-adf nebula is an intermediate-period system (NGC 5189 with a period of 4 d; García-Rojas et al. 2013; Manick et al. 2015) which, if the period of IC 4776 is a long as 9 d, may imply a connection between intermediate-period binaries and low nebular adfs. Furthermore, NGC 5189 is host to a [WR]-type primary (Manick et al. 2015), as has been claimed for the central star of IC 4776 (Tylenda et al. 1993). In total, this means three [WR]-type central stars are known to reside in binaries, with the two previous detections (NGC 5189 and PM 1-23) both having orbital periods longer than 1 d.[3]

The connection between intermediate periods, low adfs and [WR] central stars is, thus far, tenuous, given the extremely small number statistics involved, particularly given that we are unable to derive a definitive period for the central star of IC 4776. However, there may perhaps be reasonable physical grounds for such correlations. Manick et al. (2015) suggest that the strong winds observed in [WR] stars may help to prevent spiral-in, via pre-CE wind interaction, leading to longer post-CE periods.[4]

Should high adfs be the result of a nova-like eruption which ejects a second, chemically enriched gas phase into the nebula (Corradi et al. 2015; García-Rojas et al. 2016; Jones et al. 2016), then it is not unreasonable to expect that central stars with little hydrogen on their surfaces may be less likely to experience such outbursts (i.e. without hydrogen to burn, they do not undergo an eruption). However, one formation mechanism for such [WR] stars is to undergo some form of late thermal pulse which depletes their outer layers in hydrogen, whilst also providing an explanation for the presence of hydrogen-poor ejecta in their host nebulae (Ercolano et al. 2004). Indeed, previously connections were made between the abundance discrepancy problem and hydrogen-depleted central stars (Ercolano et al. 2004), particularly in the case of born-again central stars that are found to show some of the highest discrepancies (Wesson, Liu & Barlow 2003; Wesson et al. 2008). However, more recent studies have shown that in many cases PNe with [WR] central stars present with rather modest abundance discrepancies (García-Rojas et al. 2013).

Assuming that high adfs are the result of late ejection of low-metallicity material, it might be expected that longer period systems do not experience any post-CE mass transfer that could lead to an outburst. There is little evidence of such post-CE mass transfer in other high adf PNe; however, in NGC 6337, jets are observed to have been launched after the ejection of the CE (perhaps as a result of post-CE mass transfer; García-Díaz et al. 2009) whilst the nebular adf is observed to be highly elevated (∼30; Wesson et al. 2017). Furthermore, the possibility remains open for other systems based on the observation of near-Roche lobe filling, post-CE secondary stars (Jones et al. 2015).

Unfortunately, the adf of the only other PN known to host a [WR]-binary central star (PM 1-23) is not known, nor are the adfs of other PNe known to host long- and intermediate-period post-CE central stars (e.g. LTNF 1, Sp 1, 2MASS J19310888+4324577, MPA J1508−6455, NGC 2346 and NGC 1360). Thus, making further assessment of the possible relationships between periodicity, abundance pattern and central star type is currently impossible.

In conclusion, in spite of the laborious nature of the observations (De Marco et al. 2004), we encourage further radial velocity studies of the central stars of planetary nebulae in search of the missing population of intermediate-period post-CE binaries. As highlighted here, the pre-selection of targets based on morphology may be the most effective means of increasing the hit rate for detections. Whilst the possibility of a connection between [WR]-type central stars and intermediate periods is intriguing (as well as a possible link between [WR]-type and low adfs), a more rigorous survey of [WR] central stars (and their host nebulae) is required before any strong conclusions can be drawn. Furthermore, a connection between intermediate-period central stars and low adfs is on a similarly uncertain footing, and abundance studies of the known sample of PNe known to host binary central stars (of all periodicities) are strongly encouraged. Further observations of the central star of IC 4776 are essential in order to fully constrain its period and begin to place these nascent relationships on a stronger footing.

[3] The orbital period of the [WR] central star of PM 1-23 is given as 0.6 d by Hajduk, Zijlstra & Gesicki (2010), but further observations have shown that this is, in fact, half the orbital period (Manick et al. 2015, Miszalski et al., in preparation).

[4] A similar scenario has been suggested for the intermediate-period binary central star of NGC 2346 (V651 Mon, the period of which is 16 d; Soker 2002), but there is no indication that its central star is of the [WR]-type.

ACKNOWLEDGEMENTS

We are grateful to the referee, Orsola De Marco, for helpful comments and suggestions that further improved the paper. We would like to thank Tom Marsh for the use of his MOLLY software package and Aníbal García-Hernandez for the use of his UVES data. We thank Gloria Delgado-Inglada for fruitful discussions. This study is based on data obtained at the European Southern Observatory, Chile, under proposal numbers 097.D-0037, 091.D-0673, 089.D-0429 and 087.D-0446. This research made use of Astropy, a community-developed core Python package for Astronomy (Astropy Collaboration et al. 2013). PS acknowledges the ING Support and Research Studentship, and thanks the Polish National Center for Science (NCN) for support through grant 2015/18/A/ST9/00578. JG-R acknowledges support from Severo Ochoa Excellence Program (SEV-2015-0548) Advanced Postdoctoral Fellowship.

REFERENCES

Aller L. H., Keyes C. D., 1985, PASP, 97, 1142
Appenzeller I. et al., 1998, The Messenger, 94, 1

Astropy Collaboration et al., 2013, A&A, 558, A33
Basurah H. M., Ali A., Dopita M. A., Alsulami R., Amer M. A., Alruhaili A., 2016, MNRAS, 458, 2694
Boffin H. M. J., Miszalski B., Rauch T., Jones D., Corradi R. L. M., Napiwotzki R., Day-Jones A. C., Köppen J., 2012, Science, 338, 773
Bryce M., Lopez J. A., Holloway A. J., Meaburn J., 1997, ApJ Letters, 487, 161
Corradi R. L. M., Schwarz H. E., 1993, A&A, 268, 714
Corradi R. L. M. et al., 2011, MNRAS, 410, 1349
Corradi R. L. M., García-Rojas J., Jones D., Rodríguez-Gil P., 2015, ApJ, 803, 99
De Marco O., 2009, PASP, 121, 316
De Marco O., Soker N., 2011, PASP, 123, 402
De Marco O., Bond H. E., Harmer D., Fleming A. J., 2004, ApJ, 602, 93
De Marco O., Hillwig T. C., Smith A. J., 2008, AJ, 136, 323
De Marco O., Passy J.-C., Moe M., Herwig F., Mac Low M.-M., Paxton B., 2011, MNRAS, 411, 2277
Dekker H., D'Odorico S., Kaufer A., Delabre B., Kotzlowski H., 2000, in Iye M., Moorwood A. F., eds, Proc. SPIE Conf. Ser. Vol. 4008, Design, construction, and performance of UVES, the echelle spectrograph for the UT2 Kueyen Telescope at the ESO Paranal Observatory. SPIE, Bellingham, p. 534
Delgado-Inglada G., Rodríguez M., 2014, ApJ, 784, 173
Delgado-Inglada G., Morisset C., Stasińska G., 2014, MNRAS, 440, 536
Delgado-Inglada G., Rodríguez M., Peimbert M., Stasińska G., Morisset C., 2015, MNRAS, 449, 1797
Durand S., Acker A., Zijlstra A., 1998, A&AS, 132, 13
Ercolano B., Wesson R., Zhang Y., Barlow M. J., De Marco O., Rauch T., Liu X.-W., 2004, MNRAS, 354, 558
Frew D. J., Parker Q. A., Bojičić I. S., 2016, MNRAS, 455, 1459
García-Díaz M. T., Clark D. M., López J. A., Steffen W., Richer M. G., 2009, ApJ, 699, 1633
García-Rojas J., Peña M., Morisset C., Delgado-Inglada G., Mesa-Delgado A., Ruiz M. T., 2013, A&A, 558, A122
García-Rojas J., Corradi R. L. M., Monteiro H., Jones D., Rodríguez-Gil P., Cabrera-Lavers A., 2016, ApJ, 824, L27
García-Segura G., Villaver E., Langer N., Yoon S.-C., Manchado A., 2014, ApJ, 783, 74
Górny S. K., Perea-Calderón J. V., García-Hernández D. A., García-Lario P., Szczerba R., 2010, A&A, 516, A39
Guzman-Ramirez L., Lagadec E., Jones D., Zijlstra A. A., Gesicki K., 2014, MNRAS, 441, 364
Hajduk M., Zijlstra A. A., Gesicki K., 2010, MNRAS, 406, 626
Han Z., Podsiadlowski P., Eggleton P. P., 1995, MNRAS, 272, 800
Hillwig T. C., Jones D., Marco O. D., Bond H. E., Margheim S., Frew D., 2016, ApJ, 832, 125
Howarth I. D., 1983, MNRAS, 203, 301
Ivanova N. et al., 2013, A&ARv, 21, 59
Jones D., Boffin H. M. J., 2017, Nature Astron., 1, 0117
Jones D., Boffin H. M. J., Miszalski B., Wesson R., Corradi R. L. M., Tyndall A. A., 2014, A&A, 562, A89
Jones D., Boffin H. M. J., Rodríguez-Gil P., Wesson R., Corradi R. L. M., Miszalski B., Mohamed S., 2015, A&A, 580, A19
Jones D., Wesson R., García-Rojas J., Corradi R. L. M., Boffin H. M. J., 2016, MNRAS, 455, 3263
Jones D., Van Winckel H., Aller A., Exter K., De Marco O., 2017, A&A, 600, L9
Juan de Dios L., Rodríguez M., 2017, MNRAS, 469, 1036
Kahn F. D., West K. A., 1985, MNRAS, 212, 837
Kingsburgh R. L., Barlow M. J., 1994, MNRAS, 271, 257
Kwok S., Purton C. R., Fitzgerald P. M., 1978, ApJ, 219, 125
Liu X.-W., Storey P. J., Barlow M. J., Danziger I. J., Cohen M., Bryce M., 2000, MNRAS, 312, 585
Manick R., Miszalski B., McBride V., 2015, MNRAS, 448, 1789
Méndez R. H., Niemela V. S., 1981, ApJ, 250, 240
Miszalski B., Acker A., Moffat A. F. J., Parker Q. A., Udalski A., 2009a, A&A, 496, 813
Miszalski B., Acker A., Parker Q. A., Moffat A. F. J., 2009b, A&A, 505, 249
Miszalski B., Corradi R. L. M., Boffin H. M. J., Jones D., Sabin L., Santander-García M., Rodríguez-Gil P., Rubio-Díez M. M., 2011a, MNRAS, 413, 1264
Miszalski B., Jones D., Rodríguez-Gil P., Boffin H. M. J., Corradi R. L. M., Santander-García M., 2011b, A&A, 531, A158
Miszalski B., Boffin H. M. J., Corradi R. L. M., 2013, MNRAS, 428, L39
Miszalski B., Manick R., Mikołajewska J., Iłkiewicz K., Kamath D., Van Winckel H., 2017, MNRAS, preprint (arXiv:1703.10891)
Nebot Gómez-Morán A. et al., 2011, A&A, 536, A43
Nordhaus J., Blackman E. G., Frank A., 2007, MNRAS, 376, 599
O'Connor J. A., Redman M. P., Holloway A. J., Bryce M., López J. A., Meaburn J., 2000, ApJ, 531, 336
Parker Q. A. et al., 2006, MNRAS, 373, 79
Pasquini L. et al., 2002, The Messenger, 110, 1
Passy J.-C. et al., 2012, ApJ, 744, 52
Perea-Calderón J. V., García-Hernández D. A., García-Lario P., Szczerba R., Bobrowsky M., 2009, A&A, 495, L5
Phillips J. P., Pottasch S. R., 1984, A&A, 130, 91
Raga A. C., Esquivel A., Velázquez P. F., Cantó J., Haro-Corzo S., Riera A., Rodríguez-González A., 2009, ApJ, 707, L6
Shiber S., Kashi A., Soker N., 2017, MNRAS, 465, L54
Shortridge K. et al., 2004, Starlink User Note 86.21. Rutherford Appleton Laboratory
Soker N., 2002, MNRAS, 336, 1229
Soker N., 2006, PASP, 118, 260
Soker N., 2015, ApJ, 800, 114
Stanghellini L., Shaw R. A., Villaver E., 2008, ApJ, 689, 194
Steffen W., García-Segura G., Koning N., 2009, ApJ, 691, 696
Steffen W., Koning N., Wenger S., Morisset C., Magnor M., 2011, IEEE Trans. Vis. Comput. Graphics, 17, 454
Tocknell J., De Marco O., Wardle M., 2014, MNRAS, 439, 2014
Toonen S., Nelemans G., 2013, A&A, 557, A87
Tovmassian G. et al., 2010, ApJ, 714, 178
Tsamis Y. G., Barlow M. J., Liu X.-W., Danziger I. J., Storey P. J., 2003, MNRAS, 345, 186
Tylenda R., Acker A., Stenholm B., 1993, A&AS, 102, 595
Wang W., Liu X.-W., 2007, MNRAS, 381, 669
Wesson R., 2016, MNRAS, 456, 3774
Wesson R., Liu X.-W., Barlow M. J., 2003, MNRAS, 340, 253
Wesson R., Liu X.-W., Barlow M. J., 2005, MNRAS, 362, 424
Wesson R., Barlow M. J., Liu X.-W., Storey P. J., Ercolano B., De Marco O., 2008, MNRAS, 383, 1639
Wesson R., Stock D. J., Scicluna P., 2012, MNRAS, 422, 3516
Wesson R., Jones D., García-Rojas J., Corradi R. L. M., Boffin H. M. J., 2017, preprint (arXiv:1612.02215)
Zhang Y., Liu X.-W., Wesson R., Storey P. J., Liu Y., Danziger I. J., 2004, MNRAS, 351, 935

APPENDIX A: UVES SPECTRUM OF IC 4776

Fig. A1 shows the full UVES spectrum of IC 4776 referred to in Section 2, along with the ALFA fit overplotted. The observed and dereddened fluxes derived from the ALFA fit are presented in Table A1.

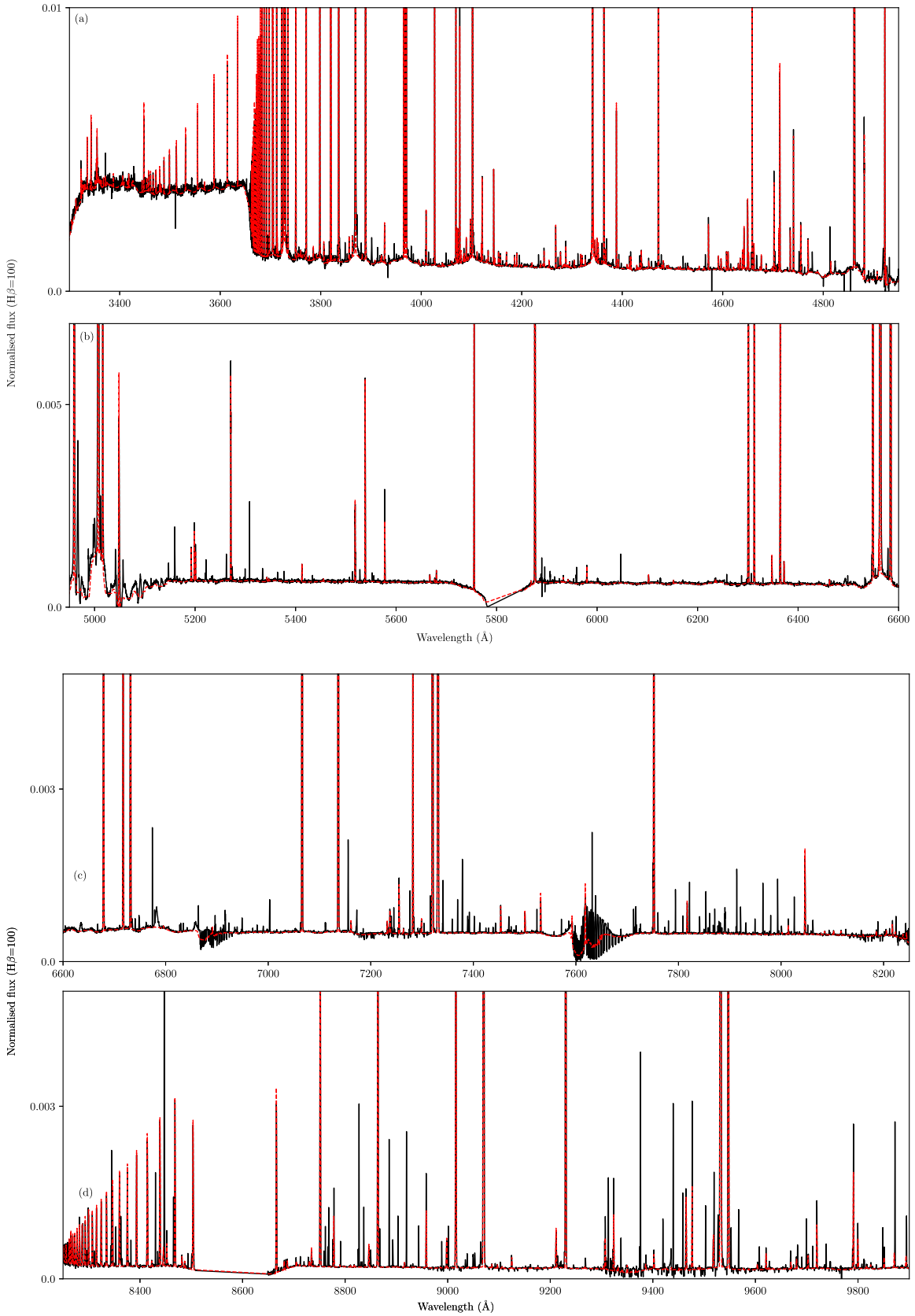

Figure A1. The ALFA spectral fit (red-dashed) overlaid on top of the combined, observed UVES spectra (black solid).

Table A1. Observed, $F(\lambda)$, and dereddened, $I(\lambda)$, nebular emission line fluxes of IC 4776 relative to $I(\mathrm{H}\beta) = 100$ ($\equiv F(\mathrm{H}\beta) = 103.992$). Asterisks denote that the line is detected as a blend with the previous line in the table, and the flux listed is the total flux of the unresolved lines. The upper and lower term columns show the upper and lower levels of the atomic transition producing the line, whilst g_1 and g_2 are the degeneracy factors of the two levels.

λ (Å)	$F(\lambda)$		$I(\lambda)$		Ion	Multiplet	Lower term	Upper term	g_1	g_2
3312.32	0.037	± 0.007	0.029	± 0.008	O III	V3	3s 3P*	3p 3S	3	3
3322.53	0.050	± 0.015	0.071	± 0.018	[Fe III]		5D	7S	9	7
3334.84	0.100	± 0.012	0.122	± 0.015	Ne II	V2	3s 4P	3p 4D*	6	8
3342.50	0.171	± 0.020	0.173	$^{+0.026}_{-0.025}$	[Ne III]		2p4 1D	2p4 1S	5	1
3353.17	0.036	± 0.011	0.060	± 0.013	[Cl III]		3p3 4S*	3p3 2P*	4	2
3354.55	0.095	± 0.014	0.127	± 0.017	He I	V8	2s 1S	7p 1P*	1	3
3355.02	0.035	± 0.014	0.060	$^{+0.016}_{-0.017}$	Ne II	V2	3s 4P	3p 4D*	4	6
3417.69	0.024	± 0.005	0.033	± 0.005	Ne II	V19	3p 2D*	3d 4F	6	8
3444.07	0.034	± 0.007	0.029	± 0.008	O III	V15	3p 3P	3d 3P*	5	5
3447.59	0.155	± 0.015	0.216	$^{+0.018}_{-0.020}$	He I	V7	2s 1S	6p 1P*	1	3
3453.32	0.013	± 0.008	0.034	± 0.009	He I	V48	2p 3P*	20d 3D	9	15
3456.86	0.054	± 0.007	0.052	$^{+0.008}_{-0.009}$	He I	V47	2p 3P*	19d 3D	9	15
3461.01	0.049	± 0.006	0.052	$^{+0.007}_{-0.008}$	He I	V46	2p 3P*	18d 3D	9	15
3465.94	0.047	± 0.011	0.050	± 0.013	He I	V45	2p 3P*	17d 2D	9	15
3471.81	0.076	± 0.008	0.063	± 0.010	He I	V44	2p 3P*	16d 3D	9	15
3478.97	0.061	± 0.009	0.067	± 0.011	He I	V43	2p 3P*	15d 3D	9	15
3487.72	0.082	± 0.009	0.095	± 0.011	He I	V42	2p 3P*	14d 3D	9	15
3498.64	0.115	± 0.013	0.111	± 0.016	He I	V40	2p 3P*	13d 3D	9	15
3512.52	0.117	± 0.012	0.132	$^{+0.014}_{-0.015}$	He I	V38	2p 3P*	12d 3D	9	15
3530.50	0.157	± 0.012	0.165	$^{+0.014}_{-0.015}$	He I	V36	2p 3P*	11d 3D	9	15
3554.42	0.203	± 0.013	0.226	$^{+0.015}_{-0.016}$	He I	V34	2p 3P*	10d 3D	9	15
3568.50	0.016	± 0.004	0.021	± 0.005	Ne II	V9	3s' 2D	3p' 2F*	6	8
3587.28	0.302	± 0.018	0.316	$^{+0.021}_{-0.023}$	He I	V31	2p 3P*	9d 3D	9	15
3613.64	0.329	± 0.017	0.369	± 0.021	He I	V6	2s 1S	5p 1P*	1	3
3634.25	0.421	± 0.021	0.473	$^{+0.025}_{-0.026}$	He I	V28	2p 3P*	8d 3D	9	15
3662.26	0.182	± 0.046	0.187	± 0.054	H I	H30	2p+ 3P*	30d+ 2D	8	*
3663.40	0.172	± 0.019	0.236	$^{+0.022}_{-0.024}$	H I	H29	2p+ 3P*	29d+ 2D	8	*
3664.68	0.275	± 0.016	0.301	$^{+0.019}_{-0.021}$	H I	H28	2p+ 3P*	28d+ 2D	8	*
3666.10	0.308	± 0.018	0.334	± 0.022	H I	H27	2p+ 2P*	27d+ 2D	8	*
3667.68	0.346	± 0.021	0.414	$^{+0.025}_{-0.027}$	H I	H26	2p+ 2P*	26d+ 2D	8	*
3669.46	0.384	± 0.024	0.416	$^{+0.028}_{-0.030}$	H I	H25	2p+ 3P*	25d+ 2D	8	*
3671.48	0.489	± 0.024	0.502	$^{+0.028}_{-0.030}$	H I	H24	2p+ 2P*	24d+ 2D	8	*
3673.74	0.539	± 0.028	0.597	$^{+0.034}_{-0.036}$	H I	H23	2p+ 2P*	23d+ 2D	8	*
3676.36	0.558	± 0.028	0.630	± 0.035	H I	H22	2p+ 2P*	22d+ 2D	8	*
3679.36	0.594	± 0.034	0.713	$^{+0.041}_{-0.044}$	H I	H21	2p+ 2P*	21d+ 2D	8	*
3682.81	0.672	± 0.039	0.776	$^{+0.046}_{-0.049}$	H I	H20	2p+ 2P*	20d+ 2D	8	*
3686.83	0.750	± 0.041	0.881	± 0.051	H I	H19	2p+ 2P*	19d+ 2D	8	*
3691.56	0.955	± 0.048	0.996	$^{+0.057}_{-0.061}$	H I	H18	2p+ 2P*	18d+ 2D	8	*
3697.15	1.023	± 0.054	1.117	$^{+0.064}_{-0.068}$	H I	H17	2p+ 2P*	17d+ 2D	8	*
3703.86	1.217	± 0.057	1.314	± 0.070	H I	H16	2p+ 2P*	16d+ 2D	8	*
3705.02	0.629	± 0.066	0.729	$^{+0.075}_{-0.076}$	He I	V25	2p 3P*	7d 3D	9	15
3711.97	1.374	± 0.070	1.534	$^{+0.083}_{-0.088}$	H I	H15	2p+ 2P*	15d+ 2D	8	*
3715.08	0.014	± 0.004	0.015	± 0.004	O III	V14	3p 3P	3d 3D*	5	7
3721.63	1.206	± 0.091	1.192	$^{+0.102}_{-0.112}$	[S III]	F2	3p2 3P	3p2 1S	3	1
3721.94	1.788	± 0.092	2.120	± 0.112	H I	H14	2p+ 2P*	14d+ 2D	8	*
3726.03	19.062	± 1.098	22.400	± 1.300	[O II]	F1	2p3 4S*	2p3 2D*	4	4
3728.82	8.352	± 0.660	9.471	$^{+0.743}_{-0.807}$	[O II]	F1	2p3 4S*	2p3 2D*	4	6
3734.37	1.754	± 0.085	2.119	$^{+0.105}_{-0.110}$	H I	H13	2p+ 2P*	13d+ 2D	8	*
3750.15	2.524	± 0.113	2.719	± 0.140	H I	H12	2p+ 2P*	12d+ 2D	8	*
3754.69	0.013	± 0.004	0.015	± 0.001	O III	V2	3s 3P*	3p 3D	3	5
3754.70	*		*		O III	V2	3s 3P*	3p 3D	3	5
3759.87	0.013	± 0.003	0.020	± 0.003	O III	V2	3s 3P*	3p 3D	5	7
3770.63	2.984	± 0.145	3.479	± 0.175	H I	H11	2p+ 2P*	11d+ 2D	8	*
3777.14	0.009	± 0.004	0.015	± 0.005	Ne II	V1	3s 4P	3p 4P*	2	4
3784.89	0.041	± 0.003	0.042	$^{+0.003}_{-0.004}$	He I ?					
3791.27	0.012	± 0.003	0.011	± 0.003	O III	V2	3s 3P*	3p 3D	5	5
3797.90	4.595	± 0.185	4.943	$^{+0.225}_{-0.236}$	H I	H10	2p+ 2P*	10d+ 2D	8	*
3805.74	0.057	± 0.008	0.059	± 0.009	He I	V58	2p 1P*	11d 1D	3	5
3819.62	1.180	± 0.030	1.254	± 0.041	He I	V22	2p 3P*	6d 3D	9	15
3645.50	0.556	± 0.008	0.644	$^{+0.016}_{-0.017}$	Balmer Jump-					

Table A1 *– continued*

λ (Å)	$F(\lambda)$		$I(\lambda)$		Ion	Multiplet	Lower term	Upper term	g_1	g_2
3646.50	0.195	± 0.006	0.222	± 0.008	Balmer Jump+					
3819.62	1.154	± 0.027	1.323	± 0.040	He I	V22	2p 3P*	6d 3D	9	15
3835.39	6.048	± 0.066	6.865	$^{+0.142}_{-0.152}$	H I	H9	2p+ 2P*	9d+ 2D	8	*
3856.02	0.082	± 0.008	0.093	± 0.002	S III	V12	3p2 2D	4p 2P*	6	4
3856.13	*		*		O II	V12	3p 4D*	3d 4D	4	2
3862.60	0.064	± 0.005	0.079	$^{+0.006}_{-0.007}$	Si II	V1	3p2 2D	4p 2P*	4	2
3868.75	70.487	± 2.963	77.200	± 3.600	[Ne III]	F1	2p4 3P	2p4 1D	5	5
3882.19	0.018	± 0.004	0.017	$^{+0.004}_{-0.005}$	O II	V12	3p 4D*	3d 4D	8	8
3888.65	4.196	± 0.368	4.954	$^{+0.411}_{-0.448}$	He I	V2	2s 3S	3p 3P*	3	9
3889.05	8.431	± 0.369	9.911	± 0.449	H I	H8	2p+ 2P*	8d+ 2D	8	*
3907.46	0.011	± 0.003	0.010	± 0.003	O II	V11	3p 4D*	3d 4P	6	6
3918.98	0.011	± 0.002	0.013	± 0.002	C II	V4	3p 2P*	4s 2S	2	2
3920.69	0.012	± 0.006	0.026	± 0.007	C II	V4	3p 2P*	4s 2S	4	2
3926.54	0.131	± 0.006	0.140	± 0.007	He I	V58	2p 1P*	8d 1D	3	5
3964.73	0.840	± 0.022	0.973	± 0.029	He I	V5	2s 1S	4p 1P*	1	3
3967.46	22.782	± 0.930	25.300	± 1.100	[Ne III]	F1	2p4 3P	2p4 1D	3	5
3970.07	13.802	± 0.234	15.258	± 0.357	H I	H7	2p+ 2P*	7d+ 2D	8	98
3994.99	0.015	± 0.003	0.014	± 0.004	N II	V12	3s 1P*	3p 1D	3	5
4009.26	0.215	± 0.018	0.188	$^{+0.019}_{-0.021}$	He I	V55	2p 1P*	7d 1D	3	5
4026.08	1.933	± 0.036	2.142	$^{+0.033}_{-0.034}$	N II	V39b	3d 3F*	4f 2[5]	7	9
4026.21	*		*		He I	V18	2p 3P*	5d 3D	9	15
4041.31	0.012	± 0.001	0.012	± 0.001	N II	V39b	3d 3F*	4f 2[5]	9	11
4043.53	0.006	± 0.002	0.007	± 0.002	N II	V39a	3d 3F*	4f 2[4]	7	9
4060.60	0.010	± 0.003	0.012	± 0.003	O II	V97	3d 2F	4f 2[4]*	8	*
4068.60	2.199	± 0.147	2.394	± 0.165	[S II]	F1	2p3 4S*	2p3 2P*	4	4
4072.16	0.115	± 0.008	0.125	$^{+0.008}_{-0.009}$	O II	V10	3p 4D*	3d 4F	6	8
4076.35	0.857	± 0.045	0.848	± 0.051	[S II]	F1	2p3 4S*	2p3 2P*	2	4
4078.84	0.035	± 0.008	0.045	± 0.009	O II	V10	3p 4D*	3d 4F	4	4
4089.29	0.074	± 0.013	0.088	± 0.014	O II	V48a	3d 4F	4f G5*	10	12
4092.93	0.014	± 0.004	0.015	± 0.004	O II	V10	3p 4D*	3d 4F	8	8
4097.25	0.129	± 0.010	0.142	± 0.002	O II	V48b	3d 4F	4f G4*	8	10
4097.26	*		*		O II	V48b	3d 4F	4f G4*	8	10
4097.33	*		*		N III	V1	3s 2S	3p 2P*	2	4
4101.74	24.309	± 0.357	26.903	± 0.536	H I	H6	2p+ 2P*	6d+ 2D	8	72
4110.78	0.028	± 0.002	0.029	$^{+0.002}_{-0.003}$	O II	V20	3p 4P*	3d 4D	4	2
4119.22	0.062	± 0.003	0.066	± 0.003	O II	V20	3p 4P*	3d 4D	6	8
4120.54	0.044	± 0.004	0.051	± 0.004	O II	V20	3p 4P*	3d 4D	6	4
4120.84	0.256	± 0.004	0.275	± 0.006	He I	V16	2p 3P*	5s 3S	9	3
4121.46	0.024	± 0.003	0.027	± 0.003	O II	V19	3p 4P*	3d 4P	2	2
4132.80	0.040	± 0.004	0.046	± 0.004	O II	V19	3p 4P*	3d 4P	2	4
4143.76	0.319	± 0.008	0.347	± 0.010	He I	V53	2p 1P*	6d 1D	3	5
4146.00	0.023	± 0.003	0.027	± 0.003	O II	V106	3p 6P	3d 6D*	8	8
4153.30	0.045	± 0.002	0.053	± 0.002	O II	V19	3p 4P*	3d 4P	4	6
4168.97	0.032	± 0.001	0.033	± 0.002	He I	V52	2p 1P*	6s 1S	3	1
4169.22	0.020	± 0.001	0.022	± 0.001	O II	V19	3p 4P*	3d 4P	6	6
4185.45	0.039	± 0.002	0.038	± 0.003	O II	V36	3p' 2F*	3d' 2G	6	8
4189.79	0.043	± 0.003	0.047	± 0.003	O II	V36	3p' 2F*	3d' 2G	8	10
4219.74	0.015	± 0.002	0.015	± 0.002	Ne II	V52a	3d 4D	4f 2[4]*	8	10
4241.78	0.010	± 0.002	0.010	± 0.002	N II	V48b	3d 3D*	4f 1[4]	7	9
4242.49	0.009	± 0.002	0.008	± 0.002	N II	V48b	3d 3D*	4f 1<4>	7	7
4243.98	0.061	± 0.005	0.061	$^{+0.005}_{-0.006}$	[Fe II]					
4253.86	0.027	± 0.003	0.029	± 0.001	O II	V101	3d 2G	4f 2[5]*	10	10
4254.00	*		*		O II	V101	3d' 2G	4f' H5*	18	22
4267.15	0.148	± 0.002	0.164	± 0.003	C II	V6	3d 2D	4f 2F*	10	14
4275.55	0.030	± 0.002	0.032	± 0.002	O II	V67a	3d 4D	4f F4*	8	10
4276.28	0.013	± 0.002	0.015	± 0.003	O II	V67b	3d 4D	4f F3*	6	6
4276.75	0.051	± 0.002	0.054	± 0.002	O II	V67b	3d 4D	4f F3*	6	8
4277.43	0.010	± 0.002	0.008	± 0.002	O II	V67c	3d 4D	4f F2*	2	4
4277.89	0.003	± 0.001	0.005	$^{+0.001}_{-0.002}$	O II	V67b	3d 4D	4f F3*	8	8
4281.32	0.006	± 0.001	0.007	± 0.001	O II	V53b	3d 4P	4f D2*	6	6
4282.96	0.009	± 0.001	0.009	± 0.002	O II	V67c	3d 4D	4f F2*	4	6
4283.73	0.009	± 0.002	0.007	± 0.002	O II	V67c	3d 4D	4f F2*	4	4
4285.69	0.017	± 0.002	0.013	± 0.003	O II	V78b	3d 2F	4f F3*	6	8
4287.39	0.074	± 0.007	0.081	$^{+0.007}_{-0.008}$	[Fe II]	F7				

Table A1 – *continued*

λ (Å)	$F(\lambda)$		$I(\lambda)$		Ion	Multiplet	Lower term	Upper term	g_1	g_2
4291.25	0.011	± 0.002	0.011	± 0.002	O II	V55	3d 4P	4f G3*	6	8
4292.16	0.007	± 0.002	0.008	± 0.001	C II		4f 2F*	10g 2G	14	18
4292.21	*		*		O II	V78c	3d 2F	4f F2*	6	6
4294.78	0.019	± 0.002	0.020	± 0.001	O II	V53b	3d 4P	4f D2*	4	6
4294.92	*		*		O II	V53b	3d 4P	4f D2*	4	4
4303.82	0.027	± 0.002	0.027	± 0.002	O II	V53a	3d 4P	4f D3*	6	8
4317.14	0.050	± 0.008	0.046	± 0.008	O II	V2	3s 4P	3p 4P*	2	4
4319.63	0.039	± 0.003	0.040	± 0.004	O II	V2	3s 4P	3p 4P*	4	6
4340.47	44.832	± 0.524	47.501	$^{+0.681}_{-0.691}$	H I	H5	2p+ 2P*	5d+ 2D	8	50
4345.55	0.065	± 0.010	0.069	± 0.001	O II	V2	3s 4P	3p 4P*	4	2
4345.56	*		*		O II	V2	3s 4P	3p 4P*	4	2
4349.43	0.085	± 0.004	0.090	± 0.005	O II	V2	3s 4P	3p 4P*	6	6
4351.81	0.097	± 0.013	0.078	± 0.014	[Fe II]					
4363.21	6.546	± 0.312	6.736	± 0.340	[O III]	F2	2p2 1D	2p2 1S	5	1
4366.89	0.052	± 0.005	0.056	± 0.005	N III	V2	3s 4P	3p 4P*	6	4
4387.93	0.573	± 0.011	0.607	± 0.013	He I	V51	2p 1P*	5d 1D	3	5
4409.30	0.013	± 0.001	0.013	± 0.001	Ne II	V55e	3d 4F	4f 2[5]*	8	10
4414.90	0.048	± 0.012	0.051	$^{+0.012}_{-0.013}$	O II	V5	3s 2P	3p 2D*	4	6
4416.97	0.026	± 0.014	0.049	± 0.015	O II	V5	3s 2P	3p 2D*	2	4
4428.52	0.018	± 0.002	0.019	± 0.001	Ne II	V61b	3d 2D	4f 2[3]*	6	8
4428.64	*		*		Ne II	V60c	3d 2F	4f 1[3]*	6	8
4430.94	0.006	± 0.002	0.008	± 0.002	Ne II	V61a	3d 2D	4f 2[4]*	6	8
4432.74	0.006	± 0.002	0.006	± 0.001	N II	V55b	3d 3P*	4f 2[3]	5	7
4432.75	*		*		N II	V55b	3d 3P*	4f 2[3]	5	7
4437.55	0.072	± 0.004	0.073	± 0.004	He I	V50	2p 1P*	5s 1S	3	1
4452.37	0.024	± 0.005	0.029	± 0.005	O II	V5	3s 2P	3p 2D*	4	4
4471.50	4.723	± 0.070	4.888	± 0.083	He I	V14	2p 3P*	4d 3D	9	15
4481.21	0.029	± 0.006	0.030	± 0.007	Mg II	V4	3d 2D	4f 2F*	10	14
4487.72	0.009	± 0.002	0.008	± 0.002	O II	V104	3d' 2P	4f' D2*	2	4
4488.75	0.011	± 0.002	0.008	± 0.002	[Fe II]	F6	4s 6D	4s 4F	6	6
4491.07	0.011	± 0.001	0.011	± 0.001	C II		4f 2F*	9g 2G	14	18
4491.23	*		*		O II	V86a	3d 2P	4f D3*	4	6
4510.91	0.009	± 0.002	0.008	± 0.002	N III	V3	3s' 4P*	3p' 4D	2	4
4514.86	0.010	± 0.001	0.010	± 0.001	N III	V3	3s' 4P*	3p' 4D	6	8
4518.15	0.003	± 0.001	0.005	± 0.001	N III	V3	3s' 4P*	3p' 4D	2	2
4552.53	0.009	± 0.002	0.013	± 0.003	N II	V58a	3d 1F*	4f 2[4]	7	9
4562.60	0.011	± 0.001	0.011	± 0.001	Mg I]		3s2 1S	3s3p 3P*	1	5
4571.10	0.176	± 0.014	0.168	$^{+0.014}_{-0.015}$	Mg I]		3s2 1S	3s3p 3P*	1	3
4590.97	0.045	± 0.002	0.049	± 0.002	O II	V15	3s' 2D	3p' 2F*	6	8
4596.18	0.037	± 0.004	0.036	± 0.004	O II	V15	3s' 2D	3p' 2F*	4	6
4601.48	0.010	± 0.001	0.010	± 0.001	N II	V5	3s 3P*	3p 3P	3	5
4602.13	0.010	± 0.001	0.009	± 0.001	O II	V92b	3d 2D	4f F3*	4	6
4607.03	0.069	± 0.004	0.071	± 0.001	[Fe III]	F3	3d6 5D	3d6 3F2	9	7
4607.16	*		*		N II	V5	3s 3P*	3p 3P	1	3
4609.44	0.018	± 0.003	0.022	± 0.003	O II	V92a	3d 2D	4f F4*	6	8
4610.20	0.064	± 0.002	0.067	± 0.003	O II	V92c	3d 2D	4f F2*	4	6
4613.68	0.006	± 0.001	0.006	± 0.001	O II	V92b	3d 2D	4f F3*	6	8
4613.87	*		*		N II	V5	3s 3P*	3p 3P	3	3
4621.25	0.012	± 0.003	0.012	± 0.001	O II	V92	3d 2D	4f 2[2]*	6	6
4621.39	*		*		N II	V5	3s 3P*	3p 3P	3	1
4630.54	0.020	± 0.001	0.023	± 0.002	N II	V5	3s 3P*	3p 3P	5	5
4634.14	0.039	± 0.001	0.039	± 0.002	N III	V2	3p 2P*	3d 2D	2	4
4638.86	0.066	± 0.003	0.072	± 0.003	O II	V1	3s 4P	3p 4D*	2	4
4640.64	0.071	± 0.004	0.075	± 0.004	N III	V2	3p 2P*	3d 2D	4	6
4641.81	0.157	± 0.004	0.161	± 0.001	O II	V1	3s 4P	3p 4D*	4	6
4641.84	*		*		N III	V2	3p 2P*	3d 2D	4	4
4647.42	0.010	± 0.002	0.009	± 0.002	C III	V1	3s 3S	3p 3P*	3	5
4649.13	0.253	± 0.008	0.261	± 0.008	O II	V1	3s 4P	3p 4D*	6	8
4650.84	0.055	± 0.006	0.064	± 0.006	O II	V1	3s 4P	3p 4D*	2	2
4658.10	0.870	± 0.069	0.964	$^{+0.069}_{-0.074}$	[Fe III]	F3	3d6 5D	3d6 3F2	9	9
4661.63	0.099	± 0.005	0.099	± 0.006	O II	V1	3s 4P	3p 4D*	4	4
4669.27	0.004	± 0.001	0.004	± 0.001	O II	V89b	3d 2D	4f D2*	4	6
4673.73	0.013	± 0.001	0.013	± 0.001	O II	V1	3s 4P	3p 4D*	4	2
4676.24	0.056	± 0.002	0.057	± 0.002	O II	V1	3s 4P	3p 4D*	6	6

Table A1 *– continued*

λ (Å)	$F(\lambda)$		$I(\lambda)$		Ion	Multiplet	Lower term	Upper term	g_1	g_2
4685.68	0.018	± 0.006	0.020	± 0.006	He II	3.4	3d+ 2D	4f+ 2F*	18	32
4696.35	0.008	± 0.001	0.007	± 0.001	O II	V1	3s 4P	3p 4D*	6	4
4699.22	0.012	± 0.002	0.015	± 0.002	O II	V25	3p 2D*	3d 2F	4	6
4701.62	0.359	± 0.022	0.335	± 0.022	[Fe III]	F3	3d6 5D	3d6 3F2	7	7
4711.37	0.158	± 0.005	0.158	± 0.005	[Ar IV]	F1	3p3 4S*	3p3 2D*	4	6
4713.17	0.744	± 0.014	0.760	± 0.015	He I	V12	2p 3P*	4s 3S	9	3
4733.91	0.152	± 0.007	0.152	± 0.008	[Fe III]	F3	3d6 5D	3d6 3F2	5	5
4740.17	0.485	± 0.022	0.514	± 0.023	[Ar IV]	F1	3p3 4S*	3p3 2D*	4	4
4754.69	0.179	± 0.013	0.181	± 0.001	[Fe III]	F 3				
4754.70	*		*		[Fe III]	F 3				
4769.40	0.125	± 0.008	0.126	± 0.008	[Fe III]	F 3				
4788.13	0.008	± 0.001	0.009	± 0.001	N II	V20	3p 3D	3d 3D*	5	5
4802.23	0.003	± 0.002	0.005	± 0.002	C II		4f 2F*	8g 2G	14	18
4803.29	0.011	± 0.002	0.009	± 0.002	N II	V20	3p 3D	3d 3D*	7	7
4814.53	0.044	± 0.002	0.043	± 0.002	[Fe II]	F20				
4815.55	0.007	± 0.002	0.006	± 0.002	S II	V9	4s 4P	4p 4S*	6	4
4861.33	103.992	± 3.705	100.000	± 4.000	H I	H4	2p+ 2P*	4d+ 2D	8	32
4881.11	0.581	± 0.050	0.512	$^{+0.048}_{-0.053}$	[Fe III]	F2	3d6 5D	3d6 3H	9	9
4906.83	0.028	± 0.005	0.029	± 0.005	[Fe IV]	V28	3p 4S*	3d 4P	4	4
4921.93	1.299	± 0.042	1.262	± 0.042	He I	V48	2p 1P*	4d 1D	3	5
4958.91	312.355	± 9.494	310.000	± 9.000	[O III]	F1	2p2 3P	2p2 1D	3	5
5006.84	952.817	± 27.604	938.000	± 27.000	[O III]	F1	2p2 3P	2p2 1D	5	5
5015.68	2.513	± 0.063	2.492	± 0.063	He I	V4	2s 1S	3p 1P*	*	1
5047.74	0.762	± 0.114	0.610	$^{+0.112}_{-0.111}$	He I	V47	2p 1P*	4s 1S	3	1
5191.82	0.088	± 0.003	0.084	± 0.003	[Ar III]	F3	2p4 1D	2p4 1S	5	1
5197.90	0.130	± 0.008	0.122	± 0.008						
5200.26	0.082	± 0.005	0.074	± 0.005	[N I]	F1	2p3 4S*	2p3 2D*	4	6
5270.40	0.531	± 0.052	0.518	$^{+0.047}_{-0.052}$	[Fe III]	F1	3d6 5D	3d6 3P2	7	5
5342.38	0.010	± 0.002	0.010	± 0.002	C II		4f 2F*	7g 2G	14	18
5345.90	0.012	± 0.002	0.008	± 0.002	[Kr IV]	F1				
5411.52	0.055	± 0.005	0.048	$^{+0.004}_{-0.005}$	He II	4.7	4f+ 2F*	7g+ 2G	32	98
5453.83	0.006	± 0.002	0.007	± 0.002	S II	V6	4s 4P	4p 4D*	6	8
5517.66	0.250	± 0.022	0.229	$^{+0.019}_{-0.021}$	[Cl III]	F1	2p3 4S*	2p3 2D*	4	6
5537.60	0.602	± 0.031	0.571	± 0.029	[Cl III]	F1	2p3 4S*	2p3 2D*	4	4
5577.34	0.206	± 0.041	0.166	$^{+0.037}_{-0.039}$	[O I]	F3	2p4 1D	2p4 1S	5	1
5666.63	0.024	± 0.002	0.022	± 0.002	N II	V3	3s 3P*	3p 3D	3	5
5676.02	0.012	± 0.002	0.010	± 0.002	N II	V3	3s 3P*	3p 3D	1	3
5679.56	0.040	± 0.002	0.034	± 0.002	N II	V3	3s 3P*	3p 3D	5	7
5686.21	0.007	± 0.002	0.005	± 0.001	N II	V3	3s 3P*	3p 3D	3	3
5710.77	0.008	± 0.002	0.007	± 0.002	N II	V3	3s 3P*	3p 3D	5	5
5754.60	1.045	± 0.089	0.909	$^{+0.080}_{-0.088}$	[N II]	F3	2p2 1D	2p2 1S	5	1
5868.00	0.012	± 0.005	0.014	± 0.005	[Kr IV]		4p3 4S	3d3 2G	4	4
5875.66	16.512	± 0.382	15.170	± 0.427	He I	V11	2p 3P*	3d 3D	9	15
5927.81	0.005	± 0.001	0.003	± 0.001	N II	V28	3p 3P	3d 3D*	1	3
5931.78	0.018	± 0.004	0.015	± 0.003	N II	V28	3p 3P	3d 3D*	3	5
5941.65	0.011	± 0.002	0.009	± 0.002	N II	V28	3p 3P	3d 3D*	5	7
5978.97	0.058	± 0.003	0.050	± 0.003	S III	V4				
6101.83	0.031	± 0.002	0.025	± 0.002	[K IV]	F1	3p4 3P	3d4 1D	5	5
6151.43	0.013	± 0.001	0.009	± 0.001	C II	V16.04	4d 2D	6f 2F*	10	14
6233.80	0.019	± 0.003	0.011	± 0.003						
6300.34	4.657	± 0.390	4.304	$^{+0.338}_{-0.367}$	[O I]	F1	2p4 3P	2p4 1D	5	5
6312.10	2.438	± 0.147	2.249	$^{+0.133}_{-0.141}$	[S III]	F3	2p2 1D	2p2 1S	5	1
6347.10	0.101	± 0.005	0.084	± 0.005	Si II	V2	4s 2S	4p 2P*	2	4
6363.78	1.694	± 0.114	1.431	± 0.103	[O I]	F1	2p4 3P	2p4 1D	3	5
6371.38	0.069	± 0.004	0.066	± 0.004	S III	V2	4s 2S	4p 2P*	2	2
6461.95	0.013	± 0.003	0.018	± 0.002	C II		4f 2F*	6g 2G	14	18
6548.10	11.700	± 0.849	9.715	$^{+0.736}_{-0.796}$	[N II]	F1	2p2 3P	2p2 1D	3	5
6560.10	0.140	± 0.042	0.115	$^{+0.035}_{-0.036}$	He II	4.6	4f+ 2F*	6g+ 2G	32	*
6562.77	345.244	± 6.736	288.000	± 5.000	H I	H3	2p+ 2P*	3d+ 2D	8	18
6583.50	39.739	± 3.370	31.100	$^{+2.800}_{-3.100}$	[N II]	F1	2p2 3P	2p2 1D	5	5
6678.16	4.886	± 0.143	4.252	± 0.164	He I	V46	2p 1P*	3d 1D	3	5
6716.44	1.734	± 0.074	1.379	$^{+0.071}_{-0.074}$	[S II]	F2	2p3 4S*	2p3 2D*	4	6
6730.82	3.537	± 0.073	2.850	± 0.098	[S II]	F2	2p3 4S*	2p3 2D*	4	4

Table A1 – *continued*

λ (Å)	$F(\lambda)$		$I(\lambda)$		Ion	Multiplet	Lower term	Upper term	g_1	g_2
6795.00	0.006	± 0.001	0.005	± 0.001	[K IV]	F1	3p4 3P	3p4 1D	3	5
7065.25	11.038	± 0.254	8.808	± 0.340	He I	V10	2p 3P*	3s 3S	9	3
7135.80	17.979	± 0.671	14.576	± 0.716	[Ar III]	F1	3p4 3P	3p4 1D	5	5
7160.56	0.033	± 0.001	0.026	± 0.001	He I		3s 3S	10p 3P*	3	9
7231.32	0.029	± 0.003	0.026	± 0.003	C II	V3	3p 2P*	3d 2D	2	4
7236.19	0.061	± 0.004	0.049	± 0.002	C II	V3	3p 2P*	3d 2D	4	6
7236.42	*		*		C II	V3	3p 2P*	3d 2D	4	6
7237.17	0.024	± 0.007	0.019	± 0.001	C II	V3	3p 2P*	3d 2D	4	4
7237.26	*		*		[Ar IV]	F2	3p3 2D*	3p3 2P*	6	4
7254.38	0.136	± 0.009	0.105	$^{+0.008}_{-0.009}$	O I	V20	3p 3P	5s 3S*	3	3
7262.76	0.014	± 0.003	0.011	± 0.002	[Ar IV]	F2	3p3 2D*	3p3 2P*	4	2
7281.35	0.936	± 0.023	0.784	± 0.032	He I	V45	2p 1P*	3s 1S	3	1
7298.04	0.041	± 0.003	0.032	± 0.003	He I		3s 3S	9p 3P*	3	9
7318.92	1.511	± 0.533	1.766	$^{+0.431}_{-0.445}$	[O II]	F2	2p3 2D*	2p3 2P*	6	2
7319.99	8.096	± 0.592	6.517	$^{+0.505}_{-0.547}$	[O II]	F2	2p3 2D*	2p3 2P*	6	4
7329.67	4.017	± 0.494	3.536	$^{+0.395}_{-0.444}$	[O II]	F2	2p3 2D*	2p3 2P*	4	2
7330.73	3.958	± 0.566	3.202	$^{+0.439}_{-0.509}$	[O II]	F2	2p3 2D*	2p3 2P*	4	4
7452.50	0.069	± 0.003	0.055	± 0.003	[Fe II]	F14				
7499.84	0.062	± 0.003	0.046	± 0.003	He I		3s 3S	8p 3P*	3	9
7530.54	0.108	± 0.004	0.086	± 0.003	[Cl IV]		3p2 3P	3p2 1D	3	5
7530.83	*		*		[Cl IV]	F1	3p2 3P	3p2 1D	3	5
7751.06	4.441	± 0.166	3.490	$^{+0.126}_{-0.131}$	[Ar III]		3p4 3P	3p4 1D	3	5
7751.12	*		*		[Ar III]	F1	3p4 3P	3p4 1D	3	5
7751.43	*		*		[Ar III]	F1	3p4 3P	3p4 1D	3	5
7816.16	0.092	± 0.003	0.072	± 0.003	He I	V69	3s 3S	7p 3P*	3	9
8014.00	0.031	± 0.006	0.020	± 0.005	N III		3p' 2D	3d' 2D*	6	4
8045.63	0.244	± 0.006	0.190	± 0.009	[Cl IV]		3p2 3P	3p2 1D	5	5
8083.88	0.009	± 0.001	0.008	± 0.001	Fe II		z4D*	d4P	4	6
8101.31	0.013	± 0.001	0.010	± 0.001	Fe III		b2D 4s3D	4P 4p5P*	5	7
8101.56	*		*		Ti III		3d5f 1F*	6g 2<4 >	7	7
8116.60	0.011	± 0.003	0.010	± 0.002	He I	3.16	3p 3P*	16d 3D	9	
8185.51	0.017	± 0.003	0.012	± 0.002	Ne I		4s 2<2 >*	7p 2<1 >	3	3
8204.42	0.013	± 0.005	0.011	± 0.004	Fe II		4P sp4P*	3F 4d4P	2	4
8215.90	0.029	± 0.009	0.026	± 0.007	N II		?	?		
8249.97	0.034	± 0.015	0.036	± 0.012	H I	P40	3d+ 2D	40f+ 2F*	18	
8255.02	0.079	± 0.014	0.042	± 0.011	H I	P38	3d+ 2D	38f+ 2F*	18	
8260.93	0.075	± 0.005	0.060	± 0.005	H I	P36	3d+ 2D	36f+ 2F*	18	
8264.28	0.113	± 0.004	0.082	± 0.005	H I	P35	3d+ 2D	35f+ 2F*	18	
8267.94	0.098	± 0.003	0.074	± 0.004	H I	P34	3d+ 2D	34f+ 2F*	18	
8271.93	0.100	± 0.002	0.076	± 0.004	H I	P33	3d+ 2D	33f+ 2F*	18	
8276.31	0.117	± 0.006	0.091	± 0.006	H I	P32	3d+ 2D	32f+ 2F*	18	
8281.12	0.137	± 0.012	0.099	$^{+0.010}_{-0.011}$	H I	P31	3d+ 2D	31f+ 2F*	18	
8286.43	0.129	± 0.010	0.101	$^{+0.008}_{-0.009}$	H I	P30	3d+ 2D	30f+ 2F*	18	
8292.31	0.159	± 0.004	0.120	± 0.006	H I	P29	3d+ 2D	29f+ 2F*	18	
8298.83	0.176	± 0.020	0.138	$^{+0.015}_{-0.017}$	H I	P28	3d+ 2D	28f+ 2F*	18	
8306.11	0.176	± 0.003	0.136	± 0.006	H I	P27	3d+ 2D	27f+ 2F*	18	
8314.26	0.196	± 0.002	0.151	± 0.006	H I	P26	3d+ 2D	26f+ 2F*	18	
8323.42	0.213	± 0.003	0.163	± 0.007	H I	P25	3d+ 2D	25f+ 2F*	18	
8333.78	0.237	± 0.003	0.183	± 0.008	H I	P24	3d+ 2D	24f+ 2F*	18	
8345.47	0.223	± 0.066	0.211	$^{+0.052}_{-0.051}$	H I	P23	3d+ 2D	23f+ 2F*	18	
8359.00	0.323	± 0.004	0.243	± 0.011	H I	P22	3d+ 2D	22f+ 2F*	18	
8374.48	0.341	± 0.004	0.258	± 0.011	H I	P21	3d+ 2D	21f+ 2F*	18	
8392.40	0.390	± 0.005	0.294	$^{+0.013}_{-0.012}$	H I	P20	3d+ 2D	20f+ 2F*	18	
8100.00	0.069	± 0.001	0.055	± 0.002	Paschen Jump-					
8400.00	0.032	± 0.003	0.024	± 0.002	Paschen Jump+					
8413.32	0.436	± 0.018	0.342	± 0.020	H I	P19	3d+ 2D	19f+ 2F*	18	
8421.99	0.020	± 0.002	0.014	± 0.001	He I	3.18	3d 3D	18p 3P*	15	
8437.95	0.508	± 0.007	0.385	± 0.017	H I	P18	3d+ 2D	18f+ 2F*	18	
8444.69	0.060	± 0.010	0.048	± 0.008	He I		3p 3P*	11d 3D	9	15
8451.20	0.056	± 0.014	0.058	± 0.011	He I	3.17	3d 3D	17p 3P*	15	
8467.25	0.633	± 0.017	0.440	$^{+0.022}_{-0.023}$	H I	P17	3d+ 2D	17f+ 2F*	18	
8480.85	0.032	± 0.003	0.028	± 0.003	[Cl III]		3p3 2D*	3p3 2P*	6	4
8486.31	0.024	± 0.001	0.018	± 0.001	He I	3.16	3d 3D	16p 3P*	15	

Table A1 *– continued*

λ (Å)	$F(\lambda)$		$I(\lambda)$		Ion	Multiplet	Lower term	Upper term	g_1	g_2
8502.48	0.501	± 0.018	0.390	$^{+0.021}_{-0.022}$	H I	P16	3d+ 2D	16f+ 2F*	18	
8665.02	0.582	± 0.023	0.429	$^{+0.025}_{-0.026}$	H I	P13	3d+ 2D	13f+ 2F*	18	
8680.28	0.029	± 0.002	0.022	± 0.001	N I	V1	3s 4P	3p 4D*	6	8
8680.53	*		*		Ca III		5d 2<4 >*	5f 2<3 >	9	7
8686.15	0.025	± 0.008	0.018	± 0.006	N I	V1	3s 4P	3p 4D*	2	4
8703.87	0.013	± 0.005	0.012	± 0.004	[Ni II]		(3F)4s 2F	(1D)4s 2D	8	6
8728.90	0.021	± 0.005	0.012	± 0.004	[Fe III]		3P4	3D	5	7
8733.43	0.056	± 0.002	0.043	$^{+0.002}_{-0.003}$	He I	3.12	3d 3D	12f 3F*	15	
8739.97	0.003	± 0.001	0.002	± 0.001	He I		3d 3D	12p 3P*	5	3
8750.47	1.393	± 0.037	1.021	± 0.053	H I	P12	3d+ 2D	12f+ 2F*	18	
8776.97	0.135	± 0.041	0.122	± 0.031	He I	3.9	3p 3P*	9d 3D	1	3
8809.83	0.003	± 0.002	0.005	± 0.001	Fe II		b4G	x4G*	12	12
8816.64	0.008	± 0.001	0.006	±0.001	He I		3p 1P*	12d 1D	3	5
8822.18	0.002	± 0.001	0.002	± 0.001	O II		4d 4F	5f G3*	6	8
8845.37	0.078	± 0.002	0.056	± 0.003	He I	3.11	3d 3D	11f 3F*	15	
8862.78	1.758	± 0.037	1.304	± 0.065	H I	P11	3d+ 2D	11f+ 2F*	18	
8899.31	0.005	± 0.001	0.003	± 0.001	C I		3d 1D*	8p 1D	5	5
8914.77	0.017	± 0.001	0.012	± 0.001	He I	3.7	3s 1S	7p 1P*	1	3
8957.25	0.158	± 0.031	0.141	$^{+0.024}_{-0.023}$	Si IV	V3.01	5s 2S	5p 2P*	2	4
8997.02	0.106	± 0.003	0.074	± 0.004	He I	3.10	3d 3D	10f 3F*	15	
9014.91	2.100	± 0.026	1.560	± 0.074	H I	P10	3d+ 2D	10f+ 2F*	18	
9068.60	36.694	± 1.484	28.800	± 1.700	[S III]		3p2 3P	3p2 1D	3	5
9084.60	0.006	± 0.002	0.008	± 0.002	Ne II		3d 4F	4p 4D*	6	4
9095.46	0.010	± 0.002	0.009	± 0.002	C I		3d 3D*	9p 3D	5	7
9123.60	0.035	± 0.007	0.027	± 0.005	[Cl II]		3p4 3P	3p4 1D	3	5
9174.49	0.007	± 0.002	0.006	± 0.002	He I	3.8	3p 3P*	8s 3S	9	3
9210.33	0.131	± 0.004	0.100	$^{+0.005}_{-0.006}$	He I	V83	3d 3D	9f 3F*	15	21
9229.01	3.056	± 0.089	2.269	$^{+0.122}_{-0.129}$	H I	P9	3d+ 2D	9f+ 2F*	18	
9323.06	0.188	± 0.053	0.139	$^{+0.039}_{-0.040}$	Fe II		e4D	5D 5p4P*	4	6
9402.17	0.051	± 0.005	0.037	± 0.004	Ne II		4f 2<4 >*	5g 1<5 >	10	12
9463.58	0.259	± 0.052	0.178	$^{+0.038}_{-0.039}$	He I	V67	3s 3S	5p 3P*	3	9
9475.03	0.266	± 0.083	0.207	$^{+0.059}_{-0.061}$	Ni II		4f 3<3 >*	3F 6d2G	8	10
9516.63	0.100	± 0.018	0.081	$^{+0.013}_{-0.014}$	He I	V76	3p 3P*	7d 3D	9	15
9530.60	92.480	± 3.012	67.600	$^{+3.900}_{-4.000}$	[S III]		3p2 3P	3p2 1D	5	5
9545.97	3.478	± 0.610	2.674	$^{+0.456}_{-0.477}$	H I	P8	3d+ 2D	8f+ 2F*	18	
9603.44	0.025	± 0.006	0.014	± 0.004	He I	V71	3s 1S	6p 1P*	1	3
9620.50	0.059	± 0.009	0.038	± 0.007	C III		3H*	3G	33	27
9702.71	0.039	± 0.014	0.030	± 0.010	He I	V75	3p 3P*	7s 3S	9	3
9720.13	0.145	± 0.029	0.105	$^{+0.021}_{-0.022}$	Ne II		4p 2S*	4d 2P	2	2
9790.52	0.256	± 0.065	0.228	$^{+0.048}_{-0.049}$	Fe II		4f 4<6 >*	5g 4<7 >	14	16
9799.26	0.094	± 0.013	0.072	$^{+0.009}_{-0.011}$	Ne II		2P*	2P	4	4
9824.13	0.013	± 0.003	0.009	± 0.002	[C I]		2p2 3P	2p2 1D	3	5
9868.21	0.056	± 0.007	0.034	± 0.005	N II	V65.09	4f 1<3 >	5g 1<4 >*	5	7
9891.09	0.025	± 0.009	0.029	± 0.007	N II	V65.11b	4f 1<4 >	5g 1<5 >*	18	27
9903.39	0.078	± 0.026	0.056	± 0.003	O II		4d 2D	5f F3*	6	6
9903.45	*		*		C II	V17.02	4f 2F*	5g 2G	22	26
9903.46	*		*		C II	V17.02	4f 2F*	5g 2G	22	26
9911.46	0.042	± 0.005	0.029	$^{+0.003}_{-0.004}$	O II		2<4 >	H<5 >*	10	10
9969.34	0.022	± 0.003	0.015	± 0.001	N II	V65.16a	4f 2<4 >	5g 2<5 >*	9	11

This paper has been typeset from a TEX/LATEX file prepared by the author.